Influence of convection on the upper tropospheric O_3 and NO_x budget in southeastern China

Xin Zhang[1,2], Yan Yin[1,2], Ronald van der A[2,3], Henk Eskes[3], Jos van Geffen[3], Yunyao Li[4], Xiang Kuang[1,2], Jeff L. Lapierre[5], Kui Chen[1,2], Zhongxiu Zhen[1,2], Jianlin Hu[1,2], Chuan He[1,2], Jinghua Chen[1,2], Rulin Shi[6], Jun Zhang[7], Xingrong Ye[7], and Hao Chen[7]

[1] Collaborative Innovation Center on Forecast and Evaluation of Meteorological Disasters/Key Laboratory for Aerosol-Cloud-Precipitation of China Meteorological Administration, Nanjing University of Information Science and Technology (NUIST), Nanjing 210044, China
[2] Department of Atmospheric Physics, Nanjing University of Information Science and Technology (NUIST), Nanjing 210044, China
[3] Royal Netherlands Meteorological Institute (KNMI), Department of Satellite Observations, De Bilt, the Netherlands
[4] Department of Atmospheric, Oceanic & Earth Sciences, George Mason University, Fairfax, VA, USA
[5] Earth Networks, Germantown, Maryland, USA
[6] Inner Mongolia Lightning Warning and Protection Center, Hohhot, 010051, China
[7] Nanjing National Reference Climatological Station, Nanjing 210044, China

Correspondence: Yan Yin (yinyan@nuist.edu.cn)

Abstract. Thunderstorms can significantly influence the air composition via strong updraft and lightning nitrogen oxides (LNO_x). In this study, the ozonesondes and TROPOMI nitrogen dioxide (NO_2) observations for two cases are combined with model to investigate the effects of typical strong convection on vertical redistribution of air pollutants in Nanjing, southeastern China. The ozonesonde observations show higher O_3 and water vapor mixing ratios in the upper troposphere (UT) after convection, indicating the strong updraft transporting lower-level airmass into the UT, and the possible downward O_3-rich air near the top of UT over the convective period. During the whole convection life cycle, the UT O_3 production is driven by the chemistry (5–10 times the magnitude of dynamic contribution) and reduced by the LNO_x (-40 %). Sensitivity tests demonstrate that neglecting LNO_x in standard TROPOMI NO_2 products causes overestimated air mass factors over fresh lightning regions and the opposite for outflow and aged lightning areas. Therefore, a new high-resolution retrieval algorithm is applied to estimate the LNO_x production efficiency. Our work shows the demand for high-resolution modeling and satellite observations on LNO_x emissions of both active and dissipated convection, especially small-scale storms.

1 Introduction

Convection can transport the surface pollutants and moisture from the planetary boundary layer to the upper troposphere (UT) in a short time, where the gaseous pollutants have a longer lifetime due to the slower reaction rates, except for photolysis, in the colder environment (Dickerson et al., 1987). As trace gases remain for more than one week in the UT, they are distributed by the upper level winds around the globe (Ridley et al., 2004). Meanwhile, the vertical profiles of trace gases are reshaped by the updraft and downdraft on timescales of hours (Huntrieser et al., 2016; Barth et al., 2019). On a global scale, the chemical

reactions of transported ozone (O_3) and its precursors can increase the amount of UT O_3 (Lawrence et al., 2003; Murray, 2016).

Nitrogen oxides (NO_x), volatile organic compounds (VOC), and hydrogen oxide radicals (HO_x) are the three main O_3 precursors, which can be uplifted or produced by thunderstorms (Bozem et al., 2017). Lightning produced nitrogen oxides (LNO_x) is the dominant natural source of UT NO_x, contributing as much as 35–45 % of global free-tropospheric ozone (Allen et al., 2010; Liaskos et al., 2015). Several lightning parameterizations have been developed for chemistry transport and climate models to evaluate the relationship between LNO_x and other trace gases (Murray et al., 2012; Gordillo-Vázquez et al., 2019; Luhar et al., 2021). Therefore, the precise estimation of LNO_x is crucial for the global O_3 trend and feedback between lightning and climate change (Finney et al., 2016; Chen et al., 2021). Globally, the LNO_x is estimated as 2–8 Tg N yr^{-1}, which is substantially less well quantified than the flash rate (Schumann and Huntrieser, 2007).

The large uncertainty of LNO_x estimation might be reduced by using cloud-resolving chemistry models in combination with satellite and aircraft observations. It is beneficial to take advantage of sonde and satellite observations for exploring the convection effects, especially for the estimation of the LNO_x production efficiency (PE). Recently, many studies have used different satellites to quantify the LNO_x PEs (Beirle et al., 2009; Pickering et al., 2016; Zhang et al., 2020). Two main methods have been proposed to distinguish LNO_x from the NO_2 background pollution: 1) subtracting the weighted temporal average NO_2 of areas with few flashes before the satellite passing time (Pickering et al., 2016; Bucsela et al., 2019; Allen et al., 2019; Lapierre et al., 2020) and 2) directly using customized lightning air mass factors (AMFs) for each convection event (Beirle et al., 2009; Zhang et al., 2020). Recently, Allen et al. (2021) proves the potential of deriving LNO_x PEs by the geostationary lightning instruments (e.g., Lightning Mapping Imager (LMI; Yang et al., 2017), Geostationary Lightning Mapper (GLM; Rudlosky et al., 2019)), and NO_2 observations such as Tropospheric Emissions: Monitoring of Pollution (TEMPO; Chance et al., 2019).

Furthermore, aircraft observations and chemical models indicate that the transport from the stratosphere to the troposphere can also increase the UT O_3 besides the chemical production from LNO_x (Pan et al., 2014). As revealed in the Deep Convective Clouds and Chemistry 2012 Studies (DC3) and mesoscale convective system simulations, the compensation of subsidence and differential advection beneath the convective core can lead to the anvil wrapping effects (Huntrieser et al., 2016; Phoenix et al., 2020). The different mechanisms of stratosphere–troposphere exchange and the effects on the tropospheric chemistry have been discussed in Holton et al. (1995) and Stohl (2003).

At present, most aircraft observations and model simulations of convection effects focus on the tropics or the United States (Vaughan et al., 2008; Barth et al., 2019). Little is known about the role of convection in southeastern China (Murray, 2016; Guo et al., 2017), where thunderstorm and lightning have increased significantly by urbanization during recent decades (Yang and Li, 2014; Pérez-Invernón et al., 2021). This is likely due to the increasing aerosol concentration, which can invigorate storms in a moist and convectively unstable environment (Koren et al., 2008; Rosenfeld et al., 2008; Tao et al., 2012). In this study, we combine ground observations and model simulations to investigate the origin of higher UT O_3 and water vapor mixing ratio (Qv) after convection, and we try to distinguish the contributions of physical processes, chemical reactions and LNO_x. For the first time, the TROPOspheric Monitoring Instrument (TROPOMI; Veefkind et al., 2012) NO_2 observations

are used to identify LNO_x PEs in southeastern China. Section 2 describes the used datasets with a brief introduction of the cloud-resolved chemistry model and the LNO_x retrieval method. Section 3 evaluates the model simulations and the physical and chemical effects of convection are analyzed in Sect. 4 and 5. We apply new a priori NO_2 profiles into the retrieval algorithm to explore the sensitivity of AMFs to LNO_x in Sect. 6. Conclusions are summarized in Sect. 7.

2 Datasets

2.1 Ozonesonde data

Five ozonesondes were launched from the Nanjing National Reference Climatological Station (31.93° N, 118.90° E) on 25 July 2019 and 01 September 2020, both days experienced strong convection. Both pre-convection and during-convection/post-convection campaigns were designed to investigate the convection effects. The convection and ozonesonde trajectories are illustrated in Fig. 1a and b.

Three Institute of Atmospheric Physics (IAP) ozonesondes had been launched near the airmass convection that developed on 25 July 2019. The IAP ozonesonde uses an electrochemical concentration cell (ECC). The complete parameters and performance are described in Zhang et al. (2014). Its average bias is less than 0.3 mPa from the surface up to 2.5 km, close to zero below 9 km, and less than 0.5 mPa between 9 km and 18 km. The first IAP ozonesonde was launched at 05:35 UTC on a sunny day (23 July) and the other two were at 05:10 UTC (pre-convection) and 06:35 UTC (post-convection) on 25 July. Because of water leakage, the pre-convection one lost signal just a few seconds after the release, and instead the ozonesonde launched on 23 July is chosen. Although the time interval is two days, the largest relative difference of forecast O_3 profiles above 10 km is usually smaller than 25 % (Fig. S2), therefore the daily variation cannot explain the observed difference of more than 65 %.

The two Vaisala ECC ozonesondes were launched successfully at 23:45 UTC 31 August (pre-convection) and 06:10 UTC 01 September (during-convection), respectively, following the standard manual to ensure the precision is better than 5 % and the accuracy is within ±(5–10) % below 30 km (Smit et al., 2007). The captured squall line was developing from the convergence of cold air and typhoon Maysak's outer region circulation. Note that the during-convection ozonesonde entered directly into the cloud, providing a unique opportunity of exploring the ozone affected by the convective clouds.

2.2 Lightning data

Three lightning datasets were used in this study: the China National Lightning Detection Network (CNLDN; Yang et al., 2015), the Earth Networks Total Lightning Network (ENTLN; Marchand et al., 2019), and the World Wide Lightning Location Network (WWLLN; Rodger et al., 2006). The detection efficiency (DE) of cloud-to-ground (CG) flashes is about 90 % for the CNLDN data in Jiangsu province ~~(?)~~ (Li et al., 2017a) while ENTLN and WWLLN detect both intra-cloud (IC) and CG flashes with specific detection frequency (1 Hz–12 MHz for ENTLN and 3–30 kHz for WWLLN). In the ENTLN data, groups of pulses are classified as a flash if they are within 700 ms and 10 km. Both strokes and lightning flashes composed of one or more strokes are included in the preprocessed data obtained from the ENTLN. The detailed processing algorithm of the

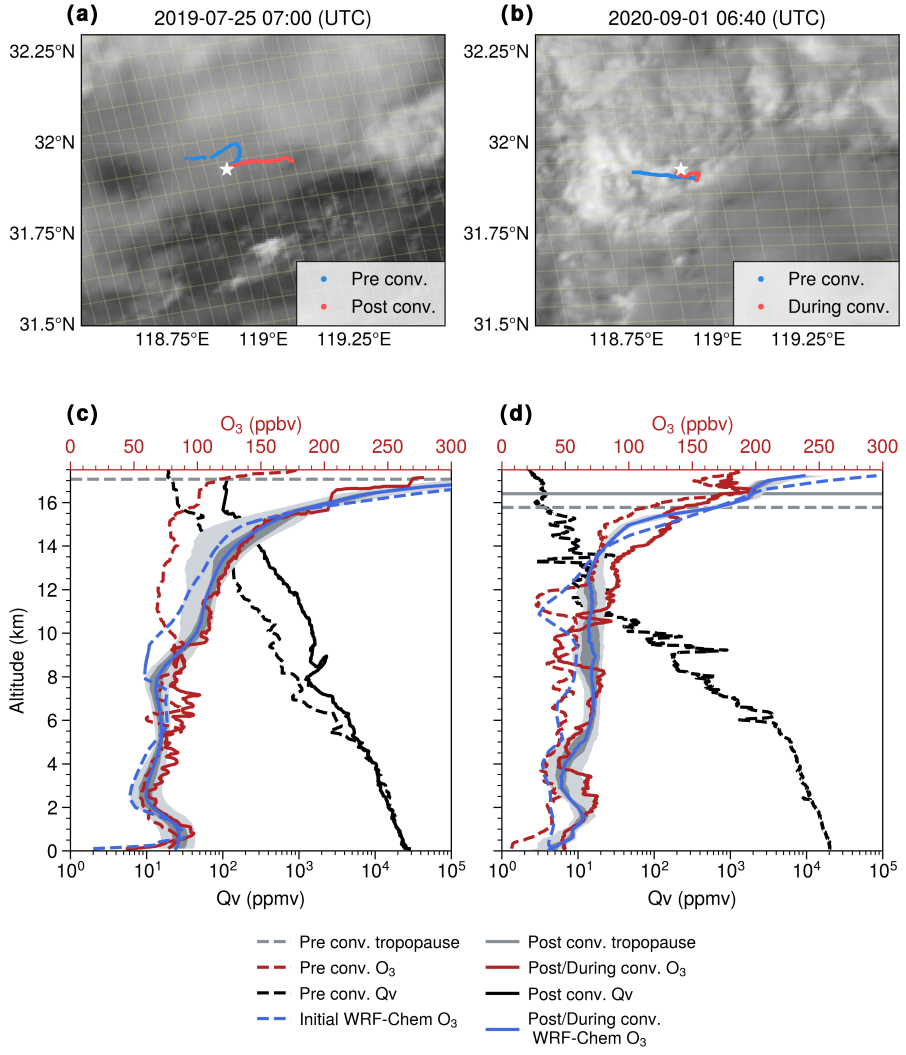

Figure 1. (a, b) The convection detected by the FY-4A Advanced Geostationary Radiation Imager (AGRI) visible channel (0.65 μm) field at the time when the post-convection/during-convection ozonesondes reached around 10 km. The pre-convection ozonesonde trajectories are colored blue while others are in red. The white star symbol stands for the observation station and the thin yellow lines are the TROPOMI swath pixels. (c) and (d) are the observed O_3 (red) and Qv (~~blue~~black) profiles in the pre-convection (dashed) and post-convection/during-convection (solid) periods. The initial (dashed) and simulated post-convection or during-convection (solid) O_3 profiles are in ~~green~~blue. The dark gray shading is the 50 % confidence interval while the light one is the 90 % confidence interval. The gray lines are the lapse rate tropopauses.

WWLLN is given by Rodger et al. (2004). The WWLLN strokes and pulses are combined with ENTLN into one dataset (ENGLN) within 10 km and 0.7 s as mentioned in Virts and Goodman (2020). To increase the lightning data coverage in our

study, the CG flashes of ENGLN and CNLDN datasets are combined using spatial and temporal clustering criteria of 10 km and 0.5 s (Zhao et al., 2020). ~~Although CG detection efficiency of ENGLN is not known for this region due to a lack of validation data, merging~~ Merging these three datasets should provide a sufficiently high CG flash detection efficiency for this analysis. Because the IC DE of all these lightning data is low in China, we conservatively use the merged CG data with a constant IC/CG ratio of 3:1 based on Wu et al. (2016) and Bandholnopparat et al. (2020). IC data will become more accurate if more Chinese total lightning networks, such as Beijing Lightning Network (BLNET; Srivastava et al., 2017), are available to be compared with lightning imaging sensors (Rudlosky and Shea, 2013; Poelman and Schulz, 2020).

2.3 TROPOMI data

On 13 October 2017, the TROPOMI on Sentinel-5 Precursor satellite was launched successfully (Veefkind et al., 2012). For the current study, we used the Royal Netherlands Meteorological Institute (KNMI) standard product v2.1-test as input to our LNO_x retrieval algorithm. A spike removal is included in the product to better deal with the detector saturation and blooming effects, which enables more valid data over the bright clouds generated by convection (Ludewig et al., 2020; van Geffen et al., 2022). Each pixel includes a slant column density quality flag (no2_scd_flag=0, see Appendix A) that can be used to get the data without known retrieval errors (Allen et al., 2021; van Geffen et al., 2022).

The official NO_2 columns are retrieved using the near-ultraviolet and visible (UV-VIS, 405–465 nm) spectrometer backscattered solar radiation measurements on the TROPOMI (van Geffen et al., 2015). The retrieval consists of three main procedures for each measured Level-1b spectrum:

1) Total NO_2 slant column density (SCD) is determined by the DOAS method.

2) The stratospheric and tropospheric SCDs are separated by data assimilation of slant columns in the Tracer Model, version 5, tailored for the application of satellite retrievals (TM5-MP; Williams et al., 2017).

3) The stratospheric and tropospheric NO_2 vertical column density (VCD) are obtained via the air mass factor (AMF) look-up tables (Lorente et al., 2017).

We replaced the tropospheric AMF (AMF_{trop}) with a new AMF called AMF for LNO_x (AMF_{LNO_x}) to derive the tropospheric LNO_x vertical column density (VCD_{LNO_x}). The concept of AMF_{LNO_x} inherits from the AMF_{trop} derived by a function of several parameters (solar zenith angle, viewing zenith angle, relative azimuth angle, surface albedo, surface pressure, cloud fraction, cloud height, and a priori trace gas profile). Briefly, the numerator is the modeled tropospheric NO_2 slant column density (SCD_{tropNO_2}) and the denominator is the modeled VCD (VCD_{NO_2} or VCD_{LNO_x}). In detail, these two AMFs can be calculated as:

$$AMF_{\mathrm{Trop}} = \frac{(1-f_r)\int_{p_{surf}}^{p_{tp}} w_{clear}(p)NO_2(p)\,dp + f_r\int_{p_{cloud}}^{p_{tp}} w_{cloudy}(p)NO_2(p)\,dp}{\int_{p_{surf}}^{p_{tp}} NO_2(p)\,dp} \quad (1)$$

$$AMF_{\mathrm{LNO_x}} = \frac{(1-f_r)\int_{p_{surf}}^{p_{tp}} w_{clear}(p)NO_2(p)\,dp + f_r\int_{p_{cloud}}^{p_{tp}} w_{cloudy}(p)NO_2(p)\,dp}{\int_{p_{surf}}^{p_{tp}} LNO_x(p)\,dp} \quad (2)$$

where p_{surf} is the surface pressure, p_{tp} is the tropopause pressure, p_{cloud} is the cloud optical pressure, f_r is the cloud radiance fraction in the NO_2 window, w_{clear} and w_{cloudy} are respectively the pressure-dependent scattering weights from the lookup table (Lorente et al., 2017) for clear and cloudy parts, and $NO_2(p)$ is the NO_2 vertical profile simulated by WRF-Chem. Besides, $LNO_x(p)$ is the LNO_x vertical profile calculated by the difference of vertical profile between WRF-Chem simulations with and without lightning. All other parameters in the KNMI v2.1-test product, including the total SCD, stratospheric SCD, total VCD, stratospheric VCD, surface albedo, and scattering weights, remain unchanged.

In comparison with this study, Pickering et al. (2016), Allen et al. (2019), Bucsela et al. (2019), and Allen et al. (2021) defined another AMF_{LNO_x} to convert SCD_{tropNO_2} to the tropospheric NO_x vertical column density (VCD_{NO_x}). Then, their VCD_{LNO_x} can be calculated as the VCD_{NO_x} subtracted by a tropospheric NO_x background. Because our AMF_{LNO_x} converts the SCD_{tropNO_2} to VCD_{LNO_x} directly, the additional estimation of background NO_2 is not needed for calculating LNO_x PE in Sect. 6.2.

2.4 Model simulations

This study uses Weather Research and Forecasting model with chemistry (WRF-Chem) version 4.1.4. The initial and boundary conditions of meteorological parameters are provided by the hourly ECMWF atmospheric reanalysis (ERA5) data (Hersbach et al., 2020). Simulations are performed with one-way nesting with 75 vertical levels and a 50 hPa model top. The domain settings are illustrated in Fig. S1. The microphysical processes are computed with the WRF Single-Moment 6-class scheme (WSM6; Hong and Lim, 2006), while the shortwave and longwave radiation is calculated by the Rapid Radiative Transfer Model for GCMs scheme (RRTMG; Iacono et al., 2008). The land surface processes are simulated by the Noah scheme (Koren et al., 1999). However, we use different planetary boundary layer (PBL) parameterizations to simulate the convection. Specifically, the 2019 case uses the Yonsei University scheme (YSU; Hong et al., 2006), while the Quasi-Normal Scale Elimination (QNSE; Sukoriansky et al., 2005) is applied to the 2020 case.

The chemical initial and boundary conditions are defined using the output from the Whole Atmosphere Community Climate Model (WACCM, https://www.acom.ucar.edu/waccm/, last access: April 12, 2022). The initial O_3 profile of the 2020 case is replaced by the O_3 profile from the ozonesonde. Anthropogenic emissions are driven by the 2016 Multi-resolution Emission Inventory for China (MEIC) version 1.3 (http://www.meicmodel.org/, last access: April 12, 2022). The Model of Emissions of Gases and Aerosol from Nature (MEGAN; Guenther et al., 2006) is used for biogenic emissions. The chemical mechanism is the Model for Ozone and Related chemical Tracers (MOZART) gas phase chemistry and Goddard Chemistry Aerosol Radiation and Transport aerosols (GOCART) for aerosols (Pfister et al., 2011). The photolysis rates are adjusted by the presence of aerosols and clouds using the new TUV photolysis option with the scaled cloud optical depth ($cloud\_fraction^{1.5}$). Note that the bimodal profile modified from the standard Ott et al. (2010) profile is employed as the vertical distribution of LNO in WRF-Chem (Laughner and Cohen, 2017), while the LNO_x parameterization is activated as 500 mol NO per flash (Zhu et al., 2019). The resulting lightning nitrogen monoxide (LNO) and lightning nitrogen dioxide (LNO_2) profiles are defined as the difference of vertical profiles between simulations with and without lightning.

To simulate the convection and LNO_x realistically, a lightning data assimilation (LDA) technique is applied to WRF-Chem. The details of the LDA technique can be found in Fierro et al. (2012) and Li et al. (2017b) and are briefly illustrated here. The water vapor mass mixing ratio is increased at constant temperature layers in columns where flashes occur:

$$Q_v = AQ_{\mathrm{sat}} + BQ_{\mathrm{sat}} \tanh(CX) \left[1 - \tanh\left(DQ_g^{\alpha}\right)\right] \tag{3}$$

where Q_{sat} is the water vapor saturation mixing ratio (g kg^{-1}), Q_g is the graupel mixing ratio (g kg^{-1}) and X is the flash rate. In our simulations, the layer between 263.15 K and 290.15 K is chosen to let the convection root in the PBL quickly as the Q_v in the lower troposphere is the deeper layer (Marchand and Fuelberg, 2014; Finney et al., 2016; Li et al., 2017b). Parameter settings follow Li et al. (2017b): A = 0.94, B = 0.2, C = 0.001 and D = 0.25 and α = 2.2. The resampled total lightning flashes data are read through the Auxiliary Input Stream of WRF every 10 minutes. For example, if the beginning time of LDA is 05:00 UTC with a time step of 10 min, all flashes in a specific grid between 05:00 and 05:10 UTC are summed as the contribution during this period. At the next time step, the flashes are classified as the next new group. Therefore, the flash count is the flash rate density (units: flashes 10 min^{-1} dx km^{-1} dy km^{-1}), where dx and dy are the resolutions of model grids in the x and y direction, respectively. This leads to flash rate densities that are the same through all nested domains as done in Fierro et al. (2012) and Li et al. (2017b), and these are used as the flash counts in the WRF-Chem directly following the method employed in CMAQ (Kang et al., 2019a, b, 2020).

3 Model evaluation

Compared with the radar observation, the simulated initiations of convection are ahead by 60 minutes and 30 minutes for the 25 July 2019 and 01 September 2020 cases, respectively (Fig. 2 and Fig. 3). The lightning assimilations are applied with the same time step forwards. For comparisons below, we choose the matched stages instead of the same time.

The airmass convection on 25 July 2019 was initialized as isolated cells. The WRF-Chem reproduces the position and intensity of isolated convections at the initial stage (Fig. 2a and 2d). At 05:40 UTC, the cells were presented with the northeast-southwest orientation and the column maximum radar reflectivity (CRF) reached 60 dBZ (Fig. 2b), which is stronger than the simulated convection (CRF = 55 dBZ, Fig. 2e). The vertical cross section of simulated radar reflectivity across the core of cells is compared with the observation (Fig. S3). Although there were much missing data caused by the long distance between convection and radar, the horizontal and vertical structures of isolated cells are roughly shown without artificial interpolation. While the simulated 45 dBZ contour extends to 12 km, the observed one only reaches 10 km because of reduced data quality above 10 km.

The squall line on 1 September, 2020 was born in the north, strengthened, and moved towards the observation site (Fig. 3). The strongest convective stage with a CRF of 60 dBZ was at 05:50 UTC which is the TROPOMI overpass time (Fig. 3b and 3e). Although the highest level reached was lower than that of 2019 case, the reflectivity in the lower troposphere (2–8 km) was larger and broader (Fig. S4). Note that the simulated dissipated cells deviate from the radar observation and this leads to the region for the ozonesonde comparison moving to the west of station (Fig. 3c and 3f).

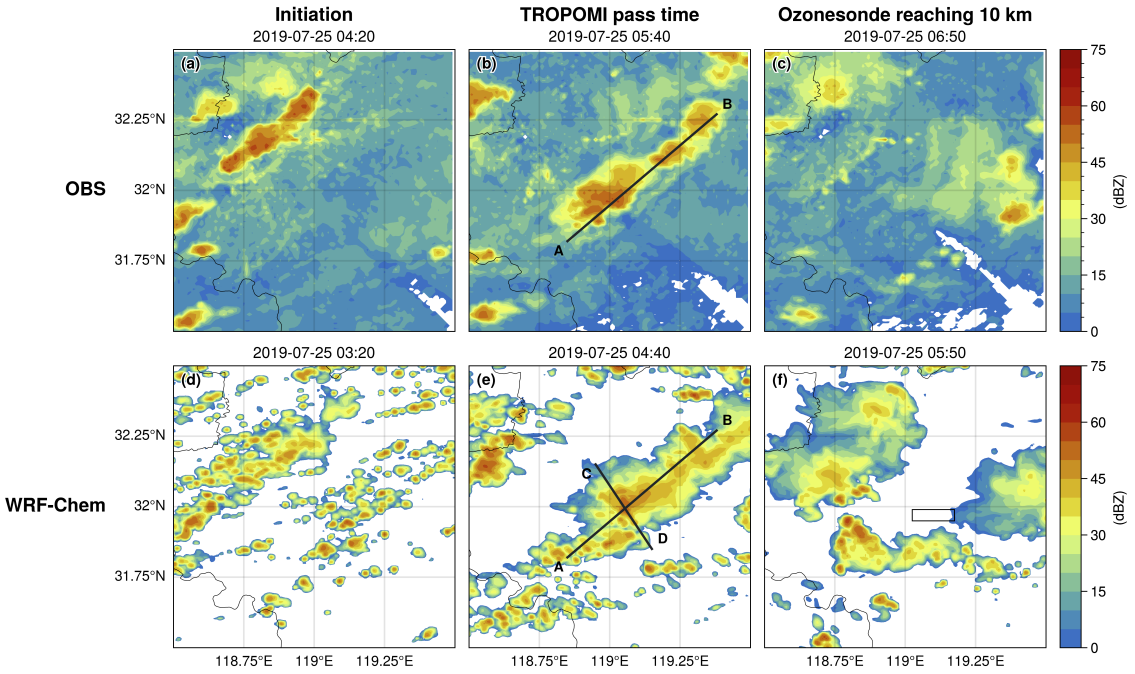

Figure 2. Observed radar composite reflectivity at (a) 04:20 UTC, (b) 05:40 UTC, and (c) 06:50 UTC. (d–e) WRF-Chem simulated composite reflectivity one hour before the radar observation times. The AB solid lines in (b) and (e) are cross section lines for Fig. S3. The CD solid line in (e) is the cross section line for Fig. 4b. The black rectangle is the region for the comparison with ozonesonde.

The measured O_3 and Qv profiles at different convection stages are shown in Fig. 1c and d. Generally, the observed UT O_3 and Qv are higher with convection, while the largest enhancements are between 10 km and 16 km. However, the 2020 case showed a larger increase in the lower troposphere (2–8 km, LT). Additionally, a two-valley shape of O_3 profile exists in both cases but at different levels: 2/8 km for the 2019 airmass and 4/10 km for the 2020 squall line. Although the WRF-Chem model tends to underestimate the O_3 concentration in the LT and UT for the 2019 and 2020 cases, respectively, it can reproduce the detailed O_3 structures and provide the opportunity to analyze the mechanisms of convection.

Three possible sources can explain the enhancements of O_3 in the UT: convective transport, chemical production, and O_3 directly produced by lightning. Only the first two factors are discussed in detail in Sect. 4, as lightning O_3 is beyond the scope of this study and still uncertain as shown by limited observations and model simulations (Morris et al., 2010; Ripoll et al., 2014).

4 Convection impacts

To evaluate the higher UT O_3 concentration after the convection, the mean vertical profiles of O_3 in the atmospheric regions passed by the ozonesondes are illustrated at three stages of convection: initiation, development, and dissipation (Fig. 4a and d).

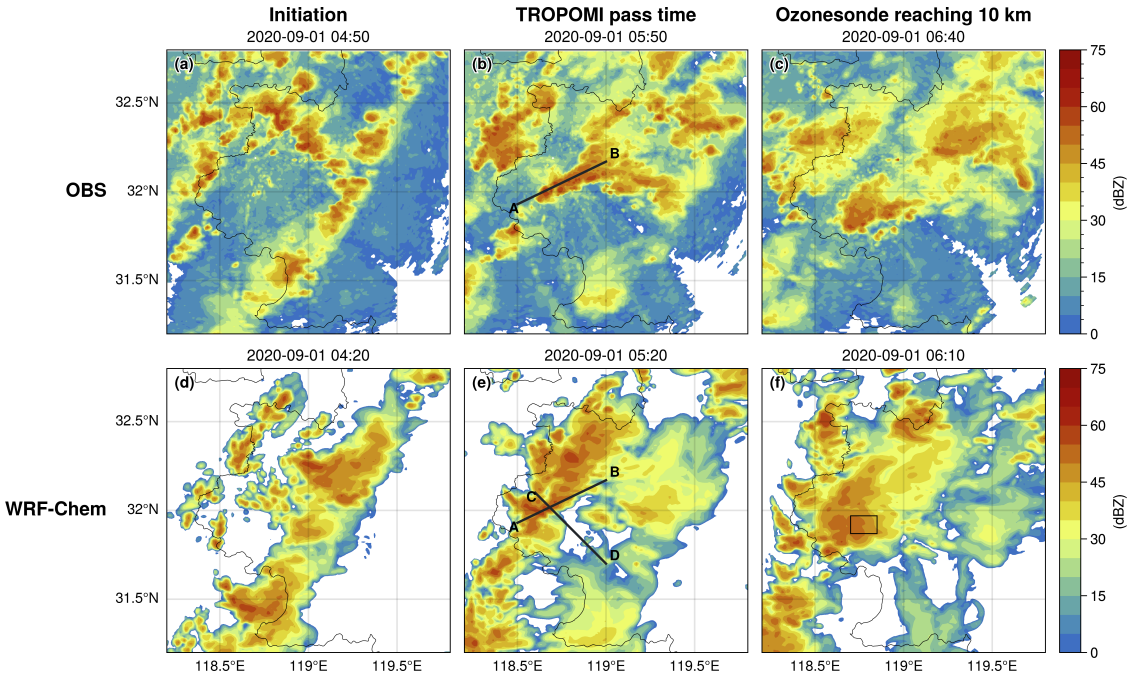

Figure 3. Same as Fig. 2 but for the case on 01 September 2020. The simulation time is 30 minutes ahead of each radar observation.

The UT O_3 increases continuously during the whole cycle of the 2020 case, but for the 2019 case, it declines at the developing stage because of the uplift of O_3-poor air while later it starts rising again. This phenomenon can be explained by the O_3 vertical cross sections at the developing stages (Fig. 4b and e). For the 2019 case, the cells of low O_3 concentration reach 16 km by the updraft, and then the high O_3 air wrapped behind the convection moves into the region. However, the observed increasing O_3 of the 2020 case is mostly from the vertically transported background O_3.

To determine the processes causing the differences between the two cases, we analyzed the outputs of mean integrated physical rates (IPR) from 10 to 14 km during the convective period (Fig. 4c and f). Generally, the opposite trend of the horizontal advection (advh) and vertical advection (advz) governs the net decrease in UT O_3 production rate of the 2019 case. Note that the advz contribution is negative between 10 and 11.5 km and positive between 11.5 and 13.8 km. This is due to the uplifted O_3-poor air and downward O_3-rich air caused by the stronger updraft compared with the 2020 case. As indicated by the higher Q_v after convection (Fig. 1c) and tropopause height (Fig. 4b), the updraft of the 2020 case is not strong enough to wrap the stratospheric O_3 like the mesoscale convective system (Phoenix et al., 2020). While the dynamic processes play an important role in the O_3 production, the positive chemistry contribution cannot be neglected in both cases and leads to the net increase in UT O_3 during the convective period of 2020 case. Specifically, the chemistry increases O_3 in both cases and the magnitude of the effect is 5–10 times that of dynamic effects. This demonstrates the dominant chemistry role in the overall effects of convection.

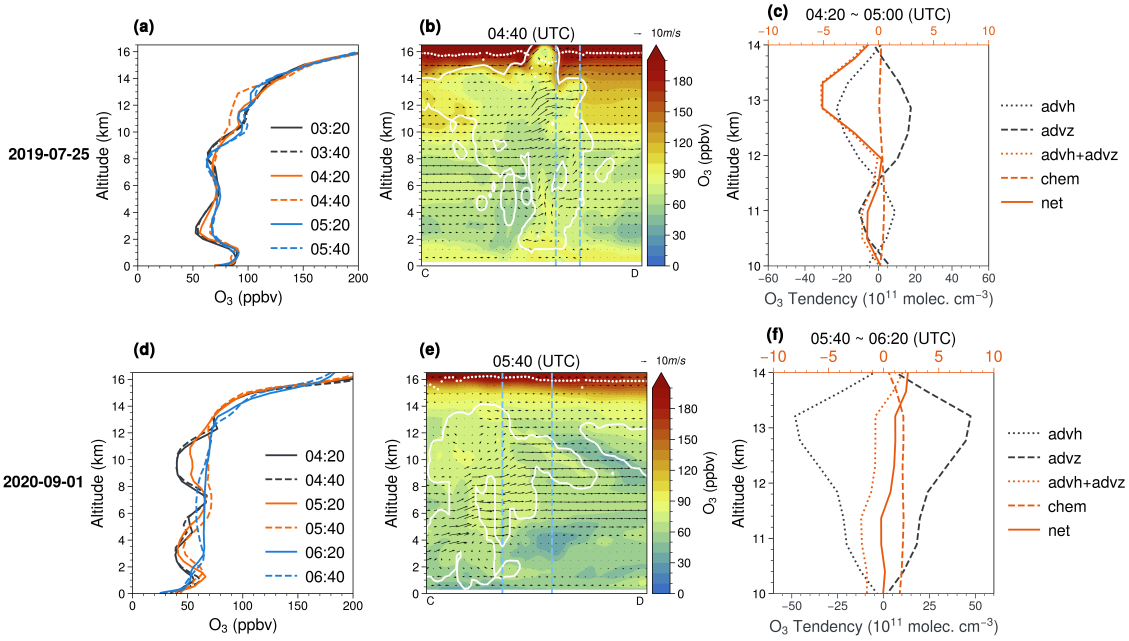

Figure 4. (a, d) The mean O_3 profiles in the regions passed by the ozonesondes at three stages: initiation (~~green~~black), development (orange), and dissipation (blue). (b, e) Vertical O_3 distribution within the convective periods along the line crossing the convective core (Fig. 2e and Fig. 3f). The blue dashed lines stand for the boundaries of regions passed by the ozonesondes, and the lapse rate tropopause is shown as the white dots. The cloud boundaries (the sum of cloud liquid water mixing ratio [q_{cloud}] and ice mixing ratio [q_{ice}] $\geq$ 0.01 g/kg) are shown in white lines. (c, f) The vertical distributions of the O_3 net production rate and tendency due to horizontal advection (advh), vertical (advz) advection, and chemistry (chem) during the convective periods.

5 Impact of lightning NO_x on the O_3 profile

Furthermore, the IPR outputs including LNO emission are compared with these excluding LNO to explore the effects of LNO_x on O_3 (Table 1). The LNO_x reduces the net O_3 production by 25 % and 40 % during the convective period and life cycle of the 2019 case, respectively. The decreased chemistry contribution is less significant ($\leq$ 1%) for the 2020 case which has a smaller lightning density near the station. Note that the LNO_x can certainly enhance the downwind ozone production on the scale of days (Pickering et al., 1996; DeCaria et al., 2005). Therefore, it is necessary to estimate the LNO_x PE accurately (discussed later in Sect. 6.2).

Additionally, the convection was divided into three regions by TROPOMI data: fresh lightning , downwind of fresh lightning, and aged lightning (See Sect. 6.1 and Fig. 8 for details). Firstly, the difference of O_3 (ΔO_3) profiles is obtained with different LNO PE assumption (Fig. 5a–c). In contrast with the net loss of ozone ($<$ 4 ppbv) over all height levels in Ott et al. (2007), the ΔO_3 is mostly positive ($<$ 1 ppbv) between 2 km and 5 km and negative ($>$ -3 ppbv) between 5 km and 12 km in our cases. The higher PE (700 mol/flash) slightly reduces the O_3 concentration by less than 1 ppbv at all levels compared with the

Table 1. Process analysis table for the mean O_3 integrated tendencies (10–14 km).

Period	Time	LNO (mol/flash)	advh + advz*	chem*	net*
Life Cycle	2019-07-25	0	-3.3 (-24.6 %)	16.7 (124.6 %)	13.4
	(03:20–05:40)	500	-2.3 (-28.8 %)	10.3 (128.8 %)	8.0
	2020-09-01	0	3.4 (9.6 %)	32.0 (90.4 %)	35.4
	(04:20–06:40)	500	4.4 (12.1 %)	31.9 (87.8 %)	36.3
Convective Period	2019-07-25	0	-19.6 (140.0 %)	5.6 (-40.0 %)	-14.0
	(04:20–05:00)	500	-20.0 (114.3 %)	2.5 (-14.3 %)	-17.5
	2020-09-01	0	-9.7 (-131.1 %)	17.1 (231.1 %)	7.4
	(05:40–06:20)	500	-10.1 (-148.5 %)	16.9 (248.5 %)	6.8

*The unit is 10^{10} molec. cm^{-3}. The percentage is the proportion of each part in the net O_3 change.

default PE (500 mol/flash) and it even leads to negative ΔO_3 between 2 km and 5 km downwind of fresh lightning (Fig. 5b). The maximum O_3 loss is between 8 km and 10 km due to the peak of LNO_x (up to 2.6 ppbv) introduced in the model.

Then, the integrated reaction rate (IRR) is applied to determine the chemistry mechanism and the effect of LNO on the O_3 variation for two layers where the ΔO_3 is opposite: 800 hPa–500 hPa ($\Delta O_3 > 0$) and 500 hPa–200 hPa ($\Delta O_3 < 0$). The tropospheric O_3 is mainly controlled by five reaction rate terms (Pickering et al., 1990; Bozem et al., 2014):

$$\begin{aligned}\frac{d}{dt}[\mathrm{O_3}] &= k_1[\mathrm{NO}][\mathrm{HO_2}] + \sum_i k_i[\mathrm{NO}][\mathrm{R_iO_2}] \\ &\quad -k_3[\mathrm{H_2O}][\mathrm{O(^1D)}] - k_4[\mathrm{HO_2}][\mathrm{O_3}] - k_5[\mathrm{OH}][\mathrm{O_3}] \end{aligned} \quad (4)$$

where k_i is the rate coefficient of the reaction between peroxy radicals (R_iO_2) and NO. The time series of each contribution to O_3 production are illustrated in Fig. 5d–i. Overall, the time series of IRR are more variable for the 2019 case due to the stronger activity as clarified in Sect. 4. The total net chemistry production of O_3 keeps positive for both layers. In detail, the reaction between NO and HO_2 always dominates the production while the oxidation of NO by RO_2 is about 40 %–60 % of that production. The dominant loss of O_3 is the photolysis (described by the reaction of $O(^1D)$ and H_2O) while the reaction between O_3 and OH is comparable during the convective period. The lowest contribution to O_3 loss, O_3 + HO_2 $\rightarrow$ OH + $2O_2$, is reduced during the convection because of the production of LNO, which captures the HO_2 reacting with O_3. Note that although the increase of total IRR induced by LNO_x can reach 1.36×10^7 molec. cm^{-3} s^{-1} and 2.60×10^6 molec. cm^{-3} s^{-1} in the low layer and high layer over these three regions, respectively, the net O_3 production actually decreases in the high layers (Fig. 5a–c) due to the combination of dynamic transport and chemical production related to LNO_x.

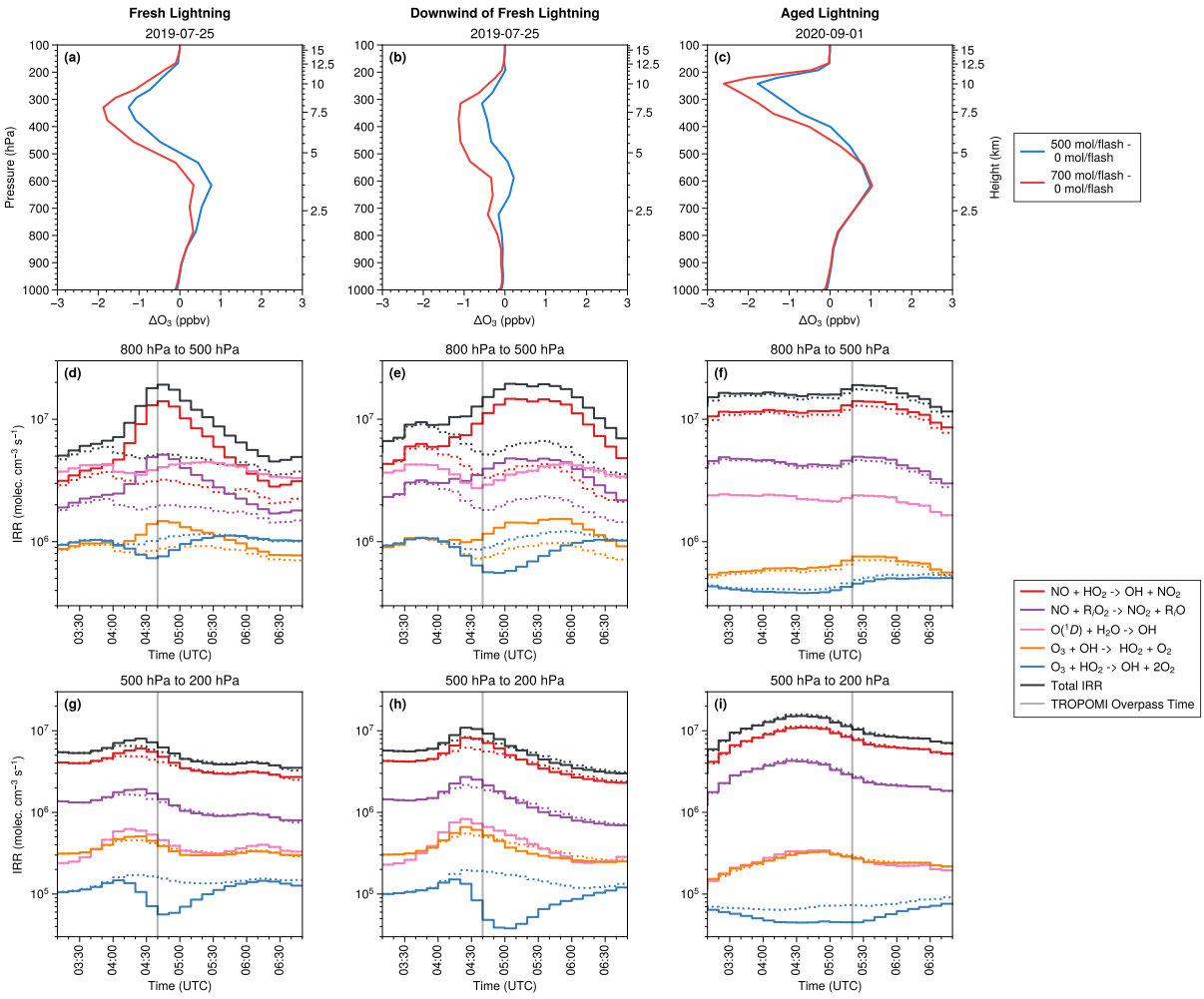

Figure 5. (a–c) Changes in O_3 profiles due to LNO_x at TROPOMI overpass time in three regions (fresh lightning region, downwind of fresh lightning, and aged lightning area) as defined in Fig. 7. (d–f) Time series of the mean integrated reaction rate (IRR) between 800 hPa and 500 hPa. The legend shows detailed species and reactions. The Total IRR is the O_3 loss IRR subtracted from the O_3 production IRR (red and ~~orange~~ purple lines). The solid line shows the IRR with LNO (500 mol/flash) while the dashed line is without LNO. (g–i) Same as (d–f) but between 500 hPa and 200 hPa.

6 TROPOMI products over the convection

6.1 Relation between lightning and TROPOMI products

As the LNO_x production estimation from TROPOMI depends upon the SCD_{tropNO_2}, we compare the SCD_{tropNO_2} distributions with the observed lightning flashes (Fig. 6a–d). Although the SCD_{tropNO_2} over the most active pixels is not valid due to the

detector saturation and blooming effect, the nearby or outflow regions still have useful data. While the flashes occurred less than 30 minutes before the TROPOMI overpass time in the 2019 case, the 2020 case had both fresh and aged LNO_2 (Fig. 6d).

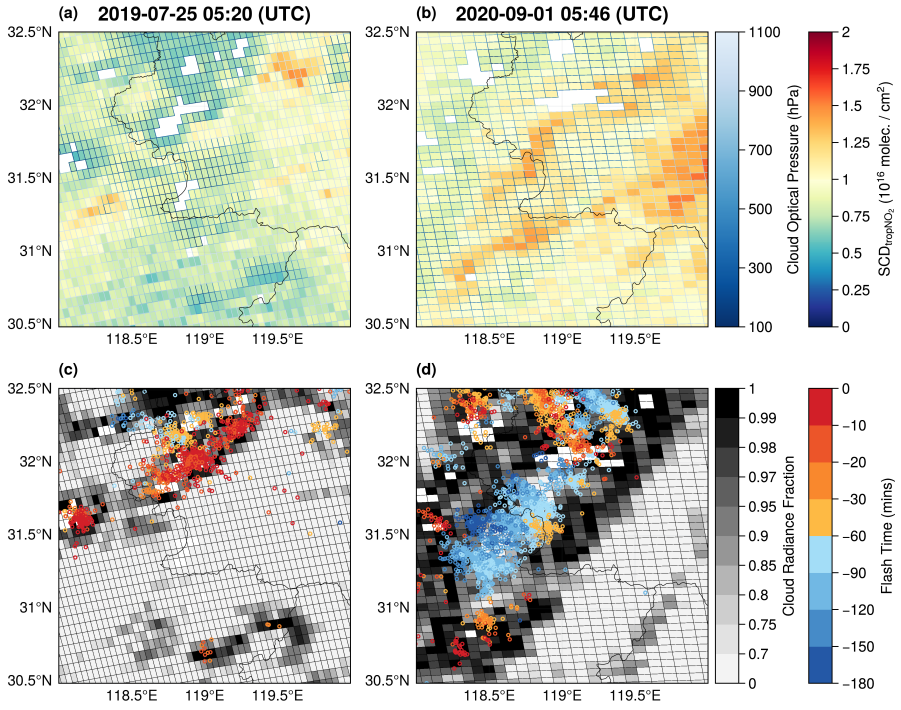

Figure 6. Events on 25 July 2019 (left) and 07 September 2020 (right). (a, b) The tropospheric NO_2 slant column density (SCD_{tropNO_2}, filled color) and cloud optical pressure (line color). These white grid cells stand for missing TROPOMI data (no2_scd_flag $\neq$ 0), as defined in Appendix A. The solid black border is Jiangsu province. (c, d) The cloud radiance fraction in the NO_2 window and flashes whose color depends on the occurring time relative to the TROPOMI overpass time. ~~The solid black border is Jiangsu province. These white grid cells stand for missing TROPOMI data (no2_scd_flag $\neq$ 0), as defined in Appendix A.~~

Specifically, the SCD_{tropNO_2} of the convective pixels ($f_r \geq 0.7$) is smaller than that in other regions. This is opposite to previous studies of large-scale convective systems with high flash density (Beirle et al., 2009). Four factors could lead to this unexpected result: the cloud top heights, flash counts, flash occurring time, and background NO_2. Either the inadequate flash or weak convection could lead to a smaller SCD_{tropNO_2} over pixels with $f_r \approx 1$ because the TROPOMI can only see the LNO_2 above the clouds. In other words, the polluted NO_2 below the broken or thinner clouds is partially exposed if $f_r < 1$. The sensitivity tests of the WRF-Chem a priori SCD_{tropNO_2} can help explain this phenomenon clearly (Fig. S5). The pixels of high SCD_{tropNO_2} with low cloud fraction belong to background NO_2 pollution (Fig. S5a and e), but the SCD_{tropNO_2} increased by UT LNO_2 is still visible compared with the lower SCD_{tropNO_2} without LNO_2 (Fig. S5b–d and f–h).

An LNO PE upper limit of 700 mol NO/flash (Ott et al., 2010) is applied to WRF-Chem for investigating the importance of LNO_x for the AMF_{trop} and AMF_{LNO_x} calculations. The changes in the retrieved AMFs are examined by replacing profiles in

three tropospheric layers independently: middle troposphere (MT, 800 hPa to 400 hPa), upper troposphere (UT, 400 hPa to 150 hPa), and troposphere (surface to tropopause). Unless otherwise specified, the changes of AMFs are obtained by increasing LNO_x in this section. Figure 7 shows that the AMF changes are mostly controlled by the LNO_x in the UT layer where the detection sensitivity is high (Beirle et al., 2009; Laughner and Cohen, 2017) and the LNO_x production reaches the peak (Fig. S6). While the AMF_{LNO_x} decreases by 5 %–40 % for both cases, the changes of AMF_{trop} (ΔAMF_{trop}) are regionally specific and can be classified by the lightning activity: fresh lightning (MT $\Delta AMF_{trop} < -20$ %), downwind of fresh lightning (MT $\Delta AMF_{trop} > 20$ %), and aged lightning (UT $\Delta AMF_{trop} > 20$ %). Figure 8a illustrates the relationship between p_{cloud} and f_r over these three regions. The clouds are higher than 400 hPa ($p_{cloud} < 400$ hPa) and f_r is larger than 0.8 over fresh lightning pixels, but both aged lightning and downwind of fresh lightning areas have clouds lower than 400 hPa. This coincides with the mean cloud pressures in Fig. S6 and explains why UT $\Delta AMF_{trop} > 20$ % exits in Fig. 7b$_i$ and b$_{iii}$, indicating the possibility of LNO_x estimations over the aged lightning regions (Sect. 6.2).

As defined in Appendix B, $SCD^{LNO_x}_{tropNO_2}/SCD^{noLNO_x}_{tropNO_2}$ and $VCD^{LNO_x}_{tropNO_2}/VCD^{noLNO_x}_{tropNO_2}$ can be used to determine which parameter controls ΔAMF_{trop}: enhanced a priori SCD_{tropNO_2} or a priori VCD_{tropNO_2} (Fig. 8b–d). Briefly, the dominant one belongs to the larger ratio. First, if the LNO_2 is included in the tropospheric layer of a priori NO_2 profiles (Fig. 7c$_i$), the AMF_{trop} decreases over most fresh lightning pixels because of the increased a priori VCD_{tropNO_2} (Fig. 8b). The situation is opposite for the downwind of the fresh lightning region. There the AMF_{trop} is larger no matter which layer is chosen (Fig. 7a$_i$–c$_i$), because the LNO_2 was convected, reached above the cloud top, and led to the larger a priori SCD_{tropNO_2} (Fig. 8c). Interestingly, for the 2020 case, the AMF_{trop} of aged lightning pixels increases more than 50 % for the UT layer (Fig. 7b$_{iii}$). It demonstrates the important role of advected UT LNO_2 and that the cloud exists as a barrier, causing the difference between a priori SCD_{tropNO_2} and a priori VCD_{tropNO_2} (Fig. 8d). Although the difference is smaller than that of the other two regions due to the LNO_2 lifetime, it is still useful for retrieving the LNO_x. Besides, considering the region-specific LNO_x effects on AMFs, we need to include the representation of LNO_2 in the TROPOMI NO_2 retrievals better, especially outflow regions. The comparisons (Fig. S6) between the TROPOMI standard NO_2 profiles from TM5-MP and WRF-Chem also illustrate the importance of LNO_x, resolved convection transport, and emissions. Aircraft observations of NO and NO_2 will be useful to determine the exact roles (Laughner and Cohen, 2017).

6.2 Estimations of LNO_x

Satellite observations with fresh convection are usually used to estimate the LNO_x PE. However, it is difficult to apply the same method to regions with small convection like the 2019 case, because of the pixel saturation of TROPOMI and limited coverage of convective area (Fig. 6c). Instead, we focus on dissipated convection which is the southern part of the 2020 case, while the northern part has multiple missing values regardless of the adequate flashes and high cloud fractions. As shown in Fig. 9b–c, the time differences between flashes and TROPOMI overpass time are longer than 30 minutes but shorter than 3 hours. Since the lifetime of NO_2 is $\sim$ 3 hours in or near the field of convection (Nault et al., 2016) and ranges from 2 to 12 h depending on

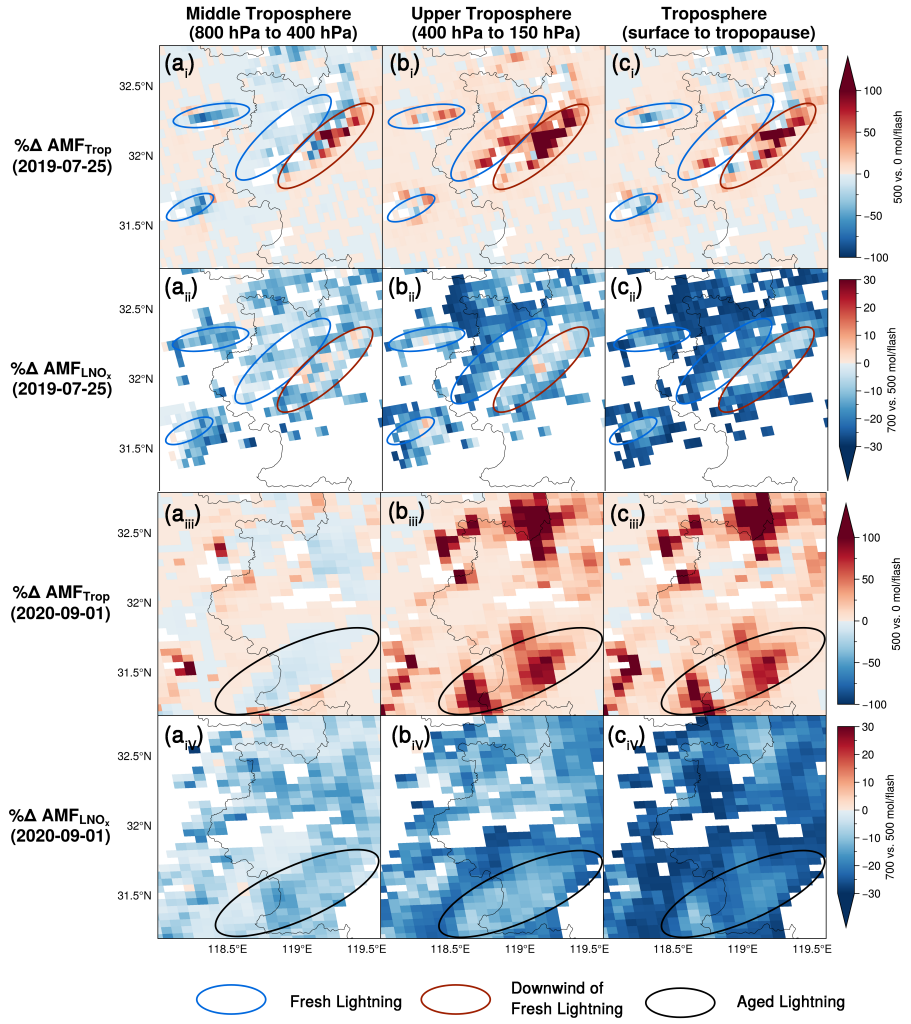

Figure 7. The percent differences of AMFs by replacing the a priori NO_2 profiles at three layers: middle troposphere (left), upper troposphere (middle), and troposphere (right). ΔAMF_{trop} is the comparison of the AMF_{trop} with 500 mol NO per flash relative to 0 mol NO per flash. ΔAMF_{LNO_x} is the comparison of the AMF_{LNO_x} with 700 mol NO per flash relative to 500 mol NO per flash. Three regions are annotated: fresh lightning (blue), downwind of fresh lightning (red), and aged lightning (~~green~~black). Because of the quite large AMF_{LNO_x} values in pixels with little lightning, ΔAMF_{LNO_x} is shown over pixels where $0 < AMF_{LNO_x} < 10$.

the convective location, these pixels can still be used for the LNO_x estimation. Equation (5) is applied to determine the mean LNO_x PE (mol/flash):

$$PE_{LNO_x} = \sum_{p} V_i A_i / \sum_{N} F_j e^{-(t_0 - t_j)/\tau} \tag{5}$$

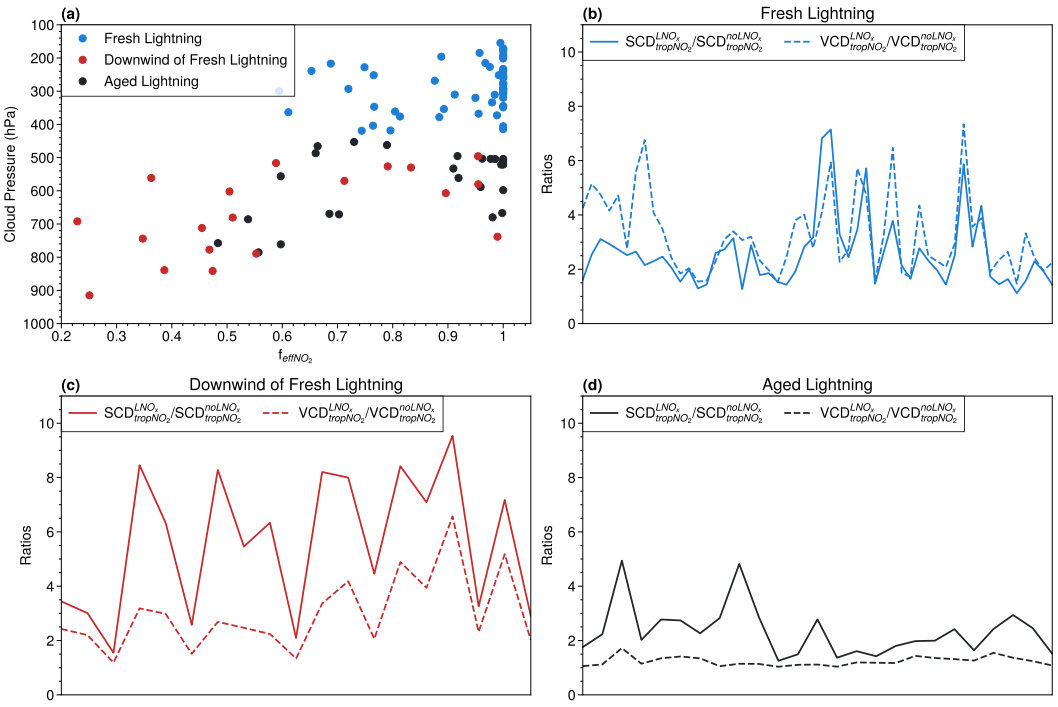

Figure 8. (a) The relationship between cloud pressure and cloud radiance fraction for three regions defined in Fig. 7: fresh lightning region, downwind of fresh lightning, and aged lightning area. (b–d) The a priori $SCD^{LNO_x}_{tropNO_2}/SCD^{noLNO_x}_{tropNO_2}$ and a priori $VCD^{LNO_x}_{tropNO_2}/VCD^{noLNO_x}_{tropNO_2}$ of pixels in these three regions. The LNO_x superscript indicates that the a priori variable is calculated with LNO_x (500 mol NO per flash) and the $noLNO_x$ superscript is without LNO_x.

where p stands for pixels affected by LNO_x, V_i (mol/m^2) is the LNO_x vertical column densities (VCD_{LNO_x} = SCD_{tropNO_2} / AMF_{LNO_x}) over pixel i with an area called A_i (m^2), N is the total number of flashes contributing to VCD_{LNO_x}, and the exponential component considers the lifetime of NO_x for each flash (F_j). Specifically, t_0 is the time of TROPOMI overpass, t_j is the time of the lightning flash, and τ represents the NO_x 3-hour lifetime near convection.

As the dissipated convection produced enough lightning and the UT winds within the storm were blowing from the west-northwest to east-southeast (Fig. 9a), the pattern of VCD_{LNO_x} can still be clearly identified (dashed rectangle in Fig. 9). Fortunately, there is a low VCD_{LNO_x} strip separating the northern and southern convection. With the careful selection, the LNO_x PE is estimated as 60 mol NO_x per flash. Although there are a few lightning flashes related to the VCD_{LNO_x} is outside of the region selection, it only affects the LNO_x PE by $\approx$ 2 mol, which is within the uncertainty discussed below.

Following Allen et al. (2019) and Zhang et al. (2020), the uncertainty of LNO_x is determined by LNO_x lifetime, lightning DE, NO/NO_2 ratio, LNO profile, and other sources (summarized in Table 2). The lifetime (τ) of NO_2 is replaced by 2 and 6 hours to evaluate the uncertainty as 27 % while another uncertainty is also 27 % related to lightning DE by changing the ratio of IC to CG to 2:1 and 4:1. The uncertainty caused by modeled NO/NO_2 ratios is assumed to be 30 % based on Allen et al.

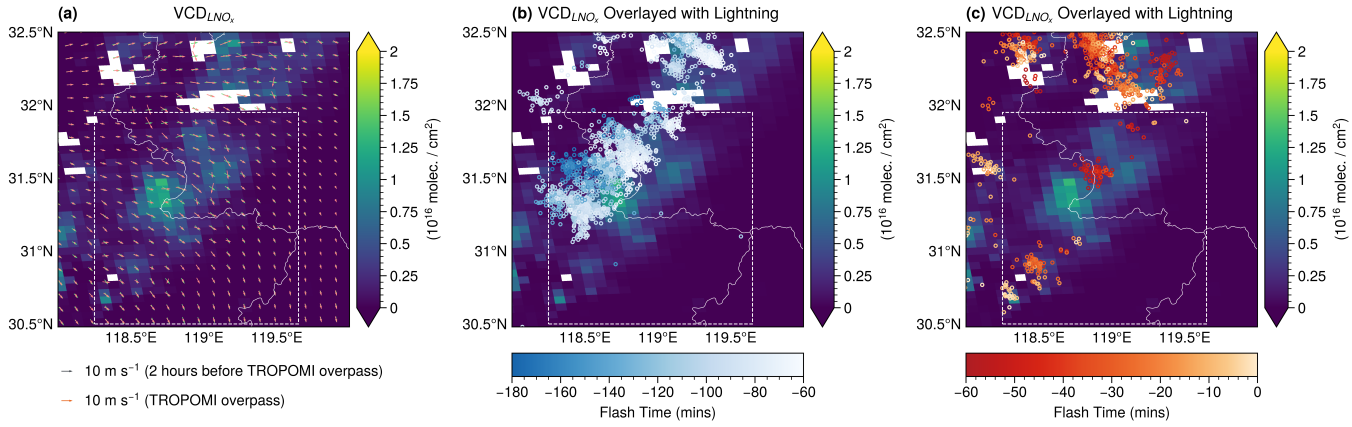

Figure 9. The background is the distribution of LNO_x vertical column densities (VCD_{LNO_x}). The white rectangles are manually selected regions for the LNO_x PE estimation. The overlayed wind arrows in (a) are the 500 hPa horizontal wind simulated by WRF-Chem. The lightning dots in (b) and (c) are the flashes whose color depends on the occurring time relative to the TROPOMI overpass time.

(2019) and the uncertainty related to LNO profile is 26 % by using the a priori NO_2 profile with 330 and 700 mol NO per flash. The uncertainty associated with the stratospheric vertical column is considered as 7 % by applying a bias of $\pm$ 10^{14} molec. cm^2 (van Geffen et al., 2022). The uncertainty caused by other possible error sources including systematic errors in slant columns, optical cloud pressure, and NO_2 redistributed by convection is difficult to quantify and assumed as 10 % following Allen et al. (2021). Assuming no correlation between errors, the total uncertainty (56 %) is estimated as the square root of the sum of the squares of all individual uncertainties. As a result, the LNO_x PE is 60 $\pm$ 33 mol NO_x per flash. It is less than that of our previous work (90 $\pm$ 50 mol NO_x per flash) over the continental United States (Zhang et al., 2020) and at the lower end of 120 $\pm$ 65 mol NO_x per flash obtained in Allen et al. (2021). Thus, more studies over China are necessary for the estimation of region-dependent LNO_x PEs.

Table 2. Uncertainties for the estimation of LNO_x production efficiency.

Type	**Uncertainty (%)**
LNO_x lifetime	27 %
Lightning detection efficiency	27 %
NO/NO_2 ratio	30 %
LNO profile	26 %
Stratospheric vertical column	7 %
Others	10 %
Net	56 %

7 Conclusions

Both the 2019 and 2020 cases saw enhanced upper tropospheric (UT) O_3 concentrations according to the ozonesonde observations. As revealed by ~~modeling using~~ the WRF-Chem model, the dynamic contribution of O_3 variation in the 2019 case was generated by mixing with the UT O_3-rich air due to strong updraft, while it was caused by vertical advection of high background O_3 in the 2020 case. The detailed analysis of integrated physical rates shows that the dynamic processes dominate the UT O_3 decrease during the convective stage of both cases. However, in the convection life cycle, the contribution of chemistry reactions to the UT O_3 production is 5–10 times that of dynamics. Besides, the UT O_3 enhancement of the 2019 case decreases by 40 % if the lightning nitrogen oxides (LNO_x) is included in the model, indicating the importance of the LNO_x. Utilizing the outputs of integrated reaction rates improves our understanding of the chemical reactions and effects of lightning nitrogen oxides (LNO_x) on O_3. While the reaction of NO and HO_2 dominates the production of O_3, the O_3 loss processes are suppressed because the LNO_x reacts with the HO_2 which is the reactant in the production.

The WRF-Chem results are incorporated into the retrieval algorithm to explore how LNO_x affects the official TROPOMI products and prove that TROPOMI is useful for LNO_x studies over small-scale convection regions. The sensitivity tests imply that air mass factors of tropospheric NO_2 are smaller for fresh lightning regions and the opposite for the aged lightning pixels or downwind of fresh lightning. The air mass factors of tropospheric LNO_x always decrease with increased LNO_x. Since the LNO_x affects the variation of tropospheric NO_2 in the outflow regions, better consideration of LNO_x is essential for studies of the tropical and mid-latitude regions in summer.

Because the saturation of TROPOMI pixels and blooming effects lead to the failure of detecting LNO_x over active convection, we focus on the dissipation regions where aged LNO_x still exists. The production efficiency is estimated to be 60 ± 33 mol LNO_x per flash, which is less than but still within the range of previous studies. Although the current results are limited, the technique can be implemented worldwide to region-specific LNO_x retrievals. To quantify and refine the LNO_x production estimates, TROPOMI data over both active and dissipated convection could provide valuable information.

Code and data availability. Data used are obtained from https://www.acom.ucar.edu/waccm/download.shtml (WACCM), http://meicmodel.org/ (MEIC), and https://www.acom.ucar.edu/wrf-chem/download.shtml (MEGAN). The relevant data and analysis code are hosted at https://github.com/zxdawn/Xin_ACP_2021_Convection_Effect (Zhang, 2021a, b). The modified WRF-Chem source code is available to the public at https://github.com/zxdawn/WRF-Chem-LDA-LFR (Zhang, 2021c). The retrieval algorithm is available at https://github.com/zxdawn/S5P-WRFChem (Zhang, 2021d).

Appendix A: Flag definitions used in this study

The no2_scd_flag is introduced to make usage of the NO_2 slant column density (SCD) data easier, by gathering information from a few variables into one flag (Table A1). This flag can thus be used for filtering, though with care as it probably does not cover all possible situation. Here "δ" refers to the SCD error (in mol/m^2) and "pqf" stands for processing quality flag.

Table A1. Definition of no2_scd_flag.

Value	Meaning
-1	no SCD value due to saturation limit exceeded, i.e. pqf=54
0	SCD with $\delta < 3.3\times10^{-5}$ & no error reported
1	SCD with $\delta < 3.3\times10^{-5}$ & error reported: pqf=55
2	SCD with $\delta < 3.3\times10^{-5}$ & other error reported, e.g. pqf=41
3	SCD with $\delta \geq 3.3\times10^{-5}$ & no error reported
4	SCD with $\delta \geq 3.3\times10^{-5}$ & error reported: pqf=55
5	SCD with $\delta \geq 3.3\times10^{-5}$ & other error reported, e.g. pqf=41
FillValue	no SCD due other error (prior to the Differential Optical Absorption Spectroscopy fit)

Appendix B: Contributions to ΔAMF$_{\text{trop}}$

In Fig. 8b–d, the contribution of LNO$_x$ to ΔAMF$_{\text{trop}}$ is divided into two parts: $\text{SCD}^{\text{LNO}_x}_{\text{tropNO}_2}/\text{SCD}^{\text{noLNO}_x}_{\text{tropNO}_2}$ and $\text{VCD}^{\text{LNO}_x}_{\text{tropNO}_2}/\text{VCD}^{\text{noLNO}_x}_{\text{tropNO}_2}$, where the LNO$_x$ superscript indicates that the a priori variable is calculated with LNO$_x$ (500 mol NO per flash) and the noLNO$_x$ superscript is without LNO$_x$. The two contributions are derived by taking the logarithm of Eq. (B1) and Eq. (B2) and then subtracting them into Eq. (B3). Here, several abbreviations are defined to simplify the symbols: S is SCD$_{\text{tropNO}_2}$, ~~V~~ V is VCD$_{\text{tropNO}_2}$, subscript 1 is with LNO$_x$, and 0 is without LNO$_x$.

$$\text{AMF}_1 = \frac{S_1}{V_1} \tag{B1}$$

$$\text{AMF}_0 = \frac{S_0}{V_0} \tag{B2}$$

$$\begin{aligned}\log(\text{AMF}_1) - \log(\text{AMF}_0) &= \log(\frac{S_1}{V_1}) - \log(\frac{S_0}{V_0}) \\ &= \log(\frac{S_1}{S_0}) - \log(\frac{V_1}{V_0})\end{aligned} \tag{B3}$$

Therefore, if $\frac{S_1}{S_0}$ is larger than $\frac{V_1}{V_0}$ (the solid line is higher than the dashed line in Fig. 8b–d), then AMF$_1$ is larger than AMF$_0$. In other words, these two variables determine how a priori LNO$_x$ affects the retrieval of NO$_2$.

Author contributions. YY directed the research and YY, XZ, and RvdA designed the research with feedback from the other co-authors; XZ, RvdA, HE, and JvG developed the retrieval algorithm; XZ modified lightning assimilation code written by YL; JLL provided guidance

and supporting data on the ENTLN data; XZ, KC, XK, ZZ, JH, CH, JZ, XY, and HC participated in the field campaigns; XZ performed simulations and analysis with the help of YY, RvdA, XK, JC, CH, and RS; XZ, YY, RvdA, and JLL interpreted the data and discussed the results. XZ drafted the manuscript with comments from the co-authors; RvdA, YY, and JLL edited the manuscript.

Competing interests. The authors declare that they have no conflict of interest.

Acknowledgements. This work is supported by the National Natural Science Foundation of China (grant nos. 91644224 and 42075067) and Postgraduate Research & Practice Innovation Program of Jiangsu Province (KYCX20_0922). We thank the Earth Networks Company for providing the Earth Networks Total Lightning Network (ENTLN) datasets. We acknowledge the use of the computational resources provided by the National Supercomputer Centre in Guangzhou (NSCC-GZ). We appreciate the discussions with Ryan M. Stauffer for ozonesonde measurements and Mary Barth for the WRF-Chem lightning NO_x module. Finally, we thank all contributors of Python packages used in this paper, especially ProPlot and Satpy (Davis, 2021; Raspaud et al., 2018, 2021).

References

Allen, D. J., Pickering, K. E., Duncan, B. N., and Damon, M.: Impact of Lightning NO Emissions on North American Photochemistry as Determined Using the Global Modeling Initiative (GMI) Model, J. Geophys. Res. Atmos., 115, 4711, https://doi.org/10.1029/2010jd014062, 2010.

Allen, D. J., Pickering, K. E., Bucsela, E., Krotkov, N., and Holzworth, R.: Lightning NO_x Production in the Tropics as Determined Using OMI NO_2 Retrievals and WWLLN Stroke Data, J. Geophys. Res. Atmos., 124, 13 498–13 518, https://doi.org/10.1029/2018JD029824, 2019.

Allen, D. J., Pickering, K. E., Bucsela, E., Geffen, J. V., Lapierre, J., Koshak, W., and Eskes, H.: Observations of Lightning NO_x Production from TROPOMI Case Studies over the United States, J. Geophys. Res. Atmos., 126, e2020JD034 174, https://doi.org/10.1029/2020JD034174, 2021.

Bandholnopparat, K., Sato, M., Adachi, T., Ushio, T., and Takahashi, Y.: Estimation of the IC to CG Ratio Using JEM-GLIMS and Ground-Based Lightning Network Data, J. Geophys. Res. Atmos., 125, e2019JD032 195, https://doi.org/10.1029/2019jd032195, 2020.

Barth, M. C., Rutledge, S. A., Brune, W. H., and Cantrell, C. A.: Introduction to the Deep Convective Clouds and Chemistry (DC3) 2012 Studies, J. Geophys. Res. Atmos., 124, 8095–8103, https://doi.org/10.1029/2019jd030944, 2019.

Beirle, S., Salzmann, M., Lawrence, M. G., and Wagner, T.: Sensitivity of Satellite Observations for Freshly Produced Lightning NO_x, Atmos. Chem. Phys., 9, 1077–1094, https://doi.org/10.5194/acp-9-1077-2009, 2009.

Bozem, H., Fischer, H., Gurk, C., Schiller, C. L., Parchatka, U., Koenigstedt, R., Stickler, A., Martinez, M., Harder, H., Kubistin, D., Williams, J., Eerdekens, G., and Lelieveld, J.: Influence of Corona Discharge on the Ozone Budget in the Tropical Free Troposphere: A Case Study of Deep Convection during GABRIEL, Atmos. Chem. Phys., 14, 8917–8931, https://doi.org/10.5194/acp-14-8917-2014, 2014.

Bozem, H., Pozzer, A., Harder, H., Martinez, M., Williams, J., Lelieveld, J., and Fischer, H.: The Influence of Deep Convection on HCHO and H_2O_2 in the Upper Troposphere over Europe, Atmos. Chem. Phys., 17, 11 835–11 848, https://doi.org/10.5194/acp-17-11835-2017, 2017.

Bucsela, E., Pickering, K. E., Allen, D., Holzworth, R., and Krotkov, N.: Midlatitude Lightning NO_x Production Efficiency Inferred from OMI and WWLLN Data, J. Geophys. Res. Atmos., 124, 13 475–13 497, https://doi.org/10.1029/2019jd030561, 2019.

Chance, K., Liu, X., Miller, C. C., González Abad, G., Huang, G., Nowlan, C., Souri, A., Suleiman, R., Sun, K., Wang, H., Zhu, L., Zoogman, P., Al-Saadi, J., Antuña-Marrero, J. C., Carr, J., Chatfield, R., Chin, M., Cohen, R., Edwards, D., Fishman, J., Flittner, D., Geddes, J., Grutter, M., Herman, J. R., Jacob, D. J., Janz, S., Joiner, J., Kim, J., Krotkov, N. A., Lefer, B., Martin, R. V., Mayol-Bracero, O. L., Naeger, A., Newchurch, M., Pfister, G. G., Pickering, K., Pierce, R. B., Rivera Cárdenas, C., Saiz-Lopez, A., Simpson, W., Spinei, E., Spurr, R. J. D., Szykman, J. J., Torres, O., and Wang, J.: TEMPO Green Paper: Chemistry, Physics, and Meteorology Experiments with the Tropospheric Emissions: Monitoring of Pollution Instrument, in: Sensors, Systems, and Next-Generation Satellites XXIII, edited by Neeck, S. P., Kimura, T., and Martimort, P., p. 10, SPIE, Strasbourg, France, https://doi.org/10.1117/12.2534883, 2019.

Chen, Y., Romps, D. M., Seeley, J. T., Veraverbeke, S., Riley, W. J., Mekonnen, Z. A., and Randerson, J. T.: Future Increases in Arctic Lightning and Fire Risk for Permafrost Carbon, Nat. Clim. Chang., https://doi.org/10.1038/s41558-021-01011-y, 2021.

Davis, L. L. B.: ProPlot, Zenodo, https://doi.org/10.5281/ZENODO.3873878, 2021.

DeCaria, A. J., Pickering, K. E., Stenchikov, G. L., and Ott, L. E.: Lightning-Generated NO_x and Its Impact on Tropospheric Ozone Production: A Three-Dimensional Modeling Study of a Stratosphere-Troposphere Experiment: Radiation, Aerosols and Ozone (STERAO-A) Thunderstorm, J. Geophys. Res. Atmos., 110, https://doi.org/10.1029/2004JD005556, 2005.

Dickerson, R. R., Huffman, G. J., Luke, W. T., Nunnermacker, L. J., Pickering, K. E., Leslie, A. C., Lindsey, C. G., Slinn, W. G., Kelly, T. J., Daum, P. H., Delany, A. C., Greenberg, J. P., Zimmerman, P. R., Boatman, J. F., Ray, J. D., and Stedman, D. H.: Thunderstorms: An Important Mechanism in the Transport of Air Pollutants, Science, 235, 460–465, https://doi.org/10.1126/science.235.4787.460, 1987.

Fierro, A. O., Mansell, E. R., Ziegler, C. L., and MacGorman, D. R.: Application of a Lightning Data Assimilation Technique in the WRF-ARW Model at Cloud-Resolving Scales for the Tornado Outbreak of 24 May 2011, Mon. Wea. Rev., 140, 2609–2627, https://doi.org/10.1175/MWR-D-11-00299.1, 2012.

Finney, D. L., Doherty, R. M., Wild, O., and Abraham, N. L.: The Impact of Lightning on Tropospheric Ozone Chemistry Using a New Global Lightning Parametrisation, Atmos. Chem. Phys., 16, 7507–7522, https://doi.org/10.5194/acp-16-7507-2016, 2016.

Gordillo-Vázquez, F. J., Pérez-Invernón, F. J., Huntrieser, H., and Smith, A. K.: Comparison of Six Lightning Parameterizations in CAM5 and the Impact on Global Atmospheric Chemistry, Earth Space Sci., 6, 2317–2346, https://doi.org/10.1029/2019ea000873, 2019.

Guenther, A., Karl, T., Harley, P., Wiedinmyer, C., Palmer, P. I., and Geron, C.: Estimates of Global Terrestrial Isoprene Emissions Using MEGAN (Model of Emissions of Gases and Aerosols from Nature), Atmos. Chem. Phys., 6, 3181–3210, https://doi.org/10.5194/acp-6-3181-2006, 2006.

Guo, F., Ju, X., Bao, M., Lu, G., Liu, Z., Li, Y., and Mu, Y.: Relationship between Lightning Activity and Tropospheric Nitrogen Dioxide and the Estimation of Lightning-Produced Nitrogen Oxides over China, Adv. Atmos. Sci., 34, 235–245, https://doi.org/10.1007/s00376-016-6087-x, 2017.

Hersbach, H., Bell, B., Berrisford, P., Hirahara, S., Horányi, A., Muñoz-Sabater, J., Nicolas, J., Peubey, C., Radu, R., Schepers, D., Simmons, A., Soci, C., Abdalla, S., Abellan, X., Balsamo, G., Bechtold, P., Biavati, G., Bidlot, J., Bonavita, M., Chiara, G., Dahlgren, P., Dee, D., Diamantakis, M., Dragani, R., Flemming, J., Forbes, R., Fuentes, M., Geer, A., Haimberger, L., Healy, S., Hogan, R. J., Hólm, E., Janisková, M., Keeley, S., Laloyaux, P., Lopez, P., Lupu, C., Radnoti, G., Rosnay, P., Rozum, I., Vamborg, F., Villaume, S., and Thépaut, J.-N.: The ERA5 Global Reanalysis, Q. J. R. Meteorol. Soc., 146, 1999–2049, https://doi.org/10.1002/qj.3803, 2020.

Holton, J. R., Haynes, P. H., McIntyre, M. E., Douglass, A. R., Rood, R. B., and Pfister, L.: Stratosphere-Troposphere Exchange, Rev. Geophys., 33, 403, https://doi.org/10.1029/95RG02097, 1995.

Hong, S. and Lim, J.: The WRF Single-Moment 6-Class Microphysics Scheme (WSM6), Asia-Pac. J. Atmospheric Sci., 42, 129–151, 2006.

Hong, S.-Y., Noh, Y., and Dudhia, J.: A New Vertical Diffusion Package with an Explicit Treatment of Entrainment Processes, Mon. Wea. Rev., 134, 2318–2341, https://doi.org/10.1175/MWR3199.1, 2006.

Huntrieser, H., Lichtenstern, M., Scheibe, M., Aufmhoff, H., Schlager, H., Pucik, T., Minikin, A., Weinzierl, B., Heimerl, K., Fütterer, D., Rappenglück, B., Ackermann, L., Pickering, K. E., Cummings, K. A., Biggerstaff, M. I., Betten, D. P., Honomichl, S., and Barth, M. C.: On the Origin of Pronounced O_3 Gradients in the Thunderstorm Outflow Region during DC3, J. Geophys. Res. Atmos., 121, 6600–6637, https://doi.org/10.1002/2015JD024279, 2016.

Iacono, M. J., Delamere, J. S., Mlawer, E. J., Shephard, M. W., Clough, S. A., and Collins, W. D.: Radiative Forcing by Long-Lived Greenhouse Gases: Calculations with the AER Radiative Transfer Models, J. Geophys. Res. Atmos., 113, https://doi.org/10.1029/2008JD009944, 2008.

Kang, D., Foley, K. M., Mathur, R., Roselle, S. J., Pickering, K. E., and Allen, D. J.: Simulating Lightning NO Production in CMAQv5.2: Performance Evaluations, Geosci. Model Dev., 12, 4409–4424, https://doi.org/10.5194/gmd-12-4409-2019, 2019a.

Kang, D., Pickering, K. E., Allen, D. J., Foley, K. M., Wong, D. C., Mathur, R., and Roselle, S. J.: Simulating Lightning NO Production in CMAQv5.2: Evolution of Scientific Updates, Geosci. Model Dev., 12, 3071–3083, https://doi.org/10.5194/gmd-12-3071-2019, 2019b.

Kang, D., Mathur, R., Pouliot, G. A., Gilliam, R. C., and Wong, D. C.: Significant Ground-Level Ozone Attributed to Lightning-Induced Nitrogen Oxides during Summertime over the Mountain West States, npj Clim. Atmos. Sci., 3, 1–7, https://doi.org/10.1038/s41612-020-0108-2, 2020.

Koren, I., Martins, J. V., Remer, L. A., and Afargan, H.: Smoke Invigoration Versus Inhibition of Clouds over the Amazon, Science, 321, 946–949, https://doi.org/10.1126/science.1159185, 2008.

Koren, V., Schaake, J., Mitchell, K., Duan, Q.-Y., Chen, F., and Baker, J. M.: A Parameterization of Snowpack and Frozen Ground Intended for NCEP Weather and Climate Models, J. Geophys. Res. Atmos., 104, 19 569–19 585, https://doi.org/10.1029/1999JD900232, 1999.

Lapierre, J. L., Laughner, J. L., Geddes, J. A., Koshak, W., Cohen, R. C., and Pusede, S. E.: Observing U.S. Regional Variability in Lightning NO_2 Production Rates, J. Geophys. Res. Atmos., 125, e2019JD031 362, https://doi.org/10.1029/2019JD031362, 2020.

Laughner, J. L. and Cohen, R. C.: Quantification of the Effect of Modeled Lightning NO_2 on UV–Visible Air Mass Factors, Atmos. Meas. Tech., 10, 4403–4419, https://doi.org/10.5194/amt-10-4403-2017, 2017.

Lawrence, M. G., Kuhlmann, R., Salzmann, M., and Rasch, P. J.: The Balance of Effects of Deep Convective Mixing on Tropospheric Ozone, Geophys. Res. Lett., 30, https://doi.org/10.1029/2003GL017644, 2003.

Li, F., Wu, L., and Li, Y.: Lightning Data Analysis of the CMA Network in China, Atmos. Meas. Tech. Discuss., pp. 1–22, https://doi.org/10.5194/amt-2016-380, 2017a.

Li, Y., Pickering, K. E., Allen, D. J., Barth, M. C., Bela, M. M., Cummings, K. A., Carey, L. D., Mecikalski, R. M., Fierro, A. O., Campos, T. L., Weinheimer, A. J., Diskin, G. S., and Biggerstaff, M. I.: Evaluation of Deep Convective Transport in Storms from Different Convective Regimes during the DC3 Field Campaign Using WRF-Chem with Lightning Data Assimilation, J. Geophys. Res. Atmos., 122, 7140–7163, https://doi.org/10.1002/2017JD026461, 2017b.

Liaskos, C. E., Allen, D. J., and Pickering, K. E.: Sensitivity of Tropical Tropospheric Composition to Lightning NO_x Production as Determined by Replay Simulations with GEOS-5, J. Geophys. Res. Atmos., 120, 8512–8534, https://doi.org/10.1002/2014JD022987, 2015.

Lorente, A., Folkert Boersma, K., Yu, H., Dörner, S., Hilboll, A., Richter, A., Liu, M., Lamsal, L. N., Barkley, M., Smedt, I., van Roozendael, M., Wang, Y., Wagner, T., Beirle, S., Lin, J.-T., Krotkov, N., Stammes, P., Wang, P., Eskes, H. J., and Krol, M.: Structural Uncertainty in Air Mass Factor Calculation for NO_2 and HCHO Satellite Retrievals, Atmos. Meas. Tech., 10, 759–782, https://doi.org/10.5194/amt-10-759-2017, 2017.

Ludewig, A., Kleipool, Q., Bartstra, R., Landzaat, R., Leloux, J., Loots, E., Meijering, P., van der Plas, E., Rozemeijer, N., Vonk, F., and Veefkind, P.: In-Flight Calibration Results of the TROPOMI Payload on Board the Sentinel-5 Precursor Satellite, Atmos. Meas. Tech., 13, 3561–3580, https://doi.org/10.5194/amt-13-3561-2020, 2020.

Luhar, A. K., Galbally, I. E., Woodhouse, M. T., and Abraham, N. L.: Assessing and Improving Cloud-Height-Based Parameterisations of Global Lightning Flash Rate, and Their Impact on Lightning-Produced NO_x and Tropospheric Composition in a Chemistry–Climate Model, Atmos. Chem. Phys., 21, 7053–7082, https://doi.org/10.5194/acp-21-7053-2021, 2021.

Marchand, M., Hilburn, K., and Miller, S. D.: Geostationary Lightning Mapper and Earth Networks Lightning Detection Over the Contiguous United States and Dependence on Flash Characteristics, J. Geophys. Res. Atmos., 124, 11 552–11 567, https://doi.org/10.1029/2019JD031039, 2019.

Marchand, M. R. and Fuelberg, H. E.: Assimilation of Lightning Data Using a Nudging Method Involving Low-Level Warming, Mon. Wea. Rev., 142, 4850–4871, https://doi.org/10.1175/MWR-D-14-00076.1, 2014.

Morris, G. A., Thompson, A. M., Pickering, K. E., Chen, S., Bucsela, E. J., and Kucera, P. A.: Observations of Ozone Production in a Dissipating Tropical Convective Cell during TC4, Atmos. Chem. Phys., 10, 11 189–11 208, https://doi.org/10.5194/acp-10-11189-2010, 2010.

Murray, L. T.: Lightning NO_x and Impacts on Air Quality, Curr. Pollution. Rep., 2, 134–134, https://doi.org/10.1007/s40726-016-0038-0, 2016.

Murray, L. T., Jacob, D. J., Logan, J. A., Hudman, R. C., and Koshak, W. J.: Optimized Regional and Interannual Variability of Lightning in a Global Chemical Transport Model Constrained by LIS/OTD Satellite Data, J. Geophys. Res. Atmos., 117, https://doi.org/10.1029/2012JD017934, 2012.

Nault, B. A., Garland, C., Wooldridge, P. J., Brune, W. H., Campuzano-Jost, P., Crounse, J. D., Day, D. A., Dibb, J., Hall, S. R., Huey, L. G., Jimenez, J. L., Liu, X., Mao, J., Mikoviny, T., Peischl, J., Pollack, I. B., Ren, X., Ryerson, T. B., Scheuer, E., Ullmann, K., Wennberg, P. O., Wisthaler, A., Zhang, L., and Cohen, R. C.: Observational Constraints on the Oxidation of NO_x in the Upper Troposphere, J. Phys. Chem. A, 120, 1468–1478, https://doi.org/10.1021/acs.jpca.5b07824, 2016.

Ott, L. E., Pickering, K. E., Stenchikov, G. L., Huntrieser, H., and Schumann, U.: Effects of Lightning NO_x Production during the 21 July European Lightning Nitrogen Oxides Project Storm Studied with a Three-Dimensional Cloud-Scale Chemical Transport Model, J. Geophys. Res. Atmos., 112, 61, https://doi.org/10.1029/2006JD007365, 2007.

Ott, L. E., Pickering, K. E., Stenchikov, G. L., Allen, D. J., DeCaria, A. J., Ridley, B., Lin, R.-F., Lang, S., and Tao, W.-K.: Production of Lightning NO_x and Its Vertical Distribution Calculated from Three-Dimensional Cloud-Scale Chemical Transport Model Simulations, J. Geophys. Res. Atmos., 115, 4711, https://doi.org/10.1029/2009JD011880, 2010.

Pan, L. L., Homeyer, C. R., Honomichl, S., Ridley, B. A., Weisman, M., Barth, M. C., Hair, J. W., Fenn, M. A., Butler, C., Diskin, G. S., Crawford, J. H., Ryerson, T. B., Pollack, I., Peischl, J., and Huntrieser, H.: Thunderstorms Enhance Tropospheric Ozone by Wrapping and Shedding Stratospheric Air, Geophys. Res. Lett., 41, 7785–7790, https://doi.org/10.1002/2014GL061921, 2014.

Pérez-Invernón, F. J., Huntrieser, H., Gordillo-Vázquez, F. J., and Soler, S.: Influence of the COVID-19 Lockdown on Lightning Activity in the Po Valley, Atmos. Res., 263, 105 808, https://doi.org/10.1016/j.atmosres.2021.105808, 2021.

Pfister, G. G., Avise, J., Wiedinmyer, C., Edwards, D. P., Emmons, L. K., Diskin, G. D., Podolske, J., and Wisthaler, A.: CO Source Contribution Analysis for California during ARCTAS-CARB, Atmos. Chem. Phys., 11, 7515–7532, https://doi.org/10.5194/acp-11-7515-2011, 2011.

Phoenix, D. B., Homeyer, C. R., Barth, M. C., and Trier, S. B.: Mechanisms Responsible for Stratosphere-to-Troposphere Transport Around a Mesoscale Convective System Anvil, J. Geophys. Res. Atmos., 125, e2019JD032 016, https://doi.org/10.1029/2019JD032016, 2020.

Pickering, K. E., Thompson, A. M., Dickerson, R. R., Luke, W. T., McNamara, D. P., Greenberg, J. P., and Zimmerman, P. R.: Model Calculations of Tropospheric Ozone Production Potential Following Observed Convective Events, J. Geophys. Res., 95, 14 049, https://doi.org/10.1029/JD095iD09p14049, 1990.

Pickering, K. E., Thompson, A. M., Wang, Y., Tao, W.-K., McNamara, D. P., Kirchhoff, V. W. J. H., Heikes, B. G., Sachse, G. W., Bradshaw, J. D., Gregory, G. L., and Blake, D. R.: Convective Transport of Biomass Burning Emissions over Brazil during TRACE A, J. Geophys. Res., 101, 23 993–24 012, https://doi.org/10.1029/96JD00346, 1996.

Pickering, K. E., Bucsela, E., Allen, D., Ring, A., Holzworth, R., and Krotkov, N.: Estimates of Lightning NO_x Production Based on OMI NO_2 Observations over the Gulf of Mexico, J. Geophys. Res. Atmos., 121, 8668–8691, https://doi.org/10.1002/2015JD024179, 2016.

Poelman, D. R. and Schulz, W.: Comparing Lightning Observations of the Ground-Based European Lightning Location System EUCLID and the Space-Based Lightning Imaging Sensor (LIS) on the International Space Station (ISS), Atmos. Meas. Tech., 13, 2965–2977, https://doi.org/10.5194/amt-13-2965-2020, 2020.

Raspaud, M., Hoese, D., Dybbroe, A., Lahtinen, P., Devasthale, A., Itkin, M., Hamann, U., Rasmussen, L. Ø., Nielsen, E. S., Leppelt, T., Maul, A., Kliche, C., and Thorsteinsson, H.: PyTroll: An Open-Source, Community-Driven Python Framework to Process Earth Observation Satellite Data, Bull. Amer. Meteor. Soc., 99, 1329–1336, https://doi.org/10.1175/bams-d-17-0277.1, 2018.

Raspaud, M., Hoese, D., Lahtinen, P., Finkensieper, S., Holl, G., Dybbroe, A., Proud, S., Meraner, A., Zhang, X., Joro, S., Roberts, W., Rasmussen, L. Ø., Joleenf, Méndez, J. H. B., Zhu, Y., Daruwala, R., Strandgren, BENR0, Jasmin, T., Barnie, T., Sigurðsson, E., R.K.Garcia, Leppelt, T., ColinDuff, Egede, U., LTMeyer, Itkin, M., Goodson, R., Radar, Satellite and Nowcasting Division, and Jkotro: Pytroll/Satpy: Version 0.25.1, Zenodo, https://doi.org/10.5281/ZENODO.4422120, 2021.

Ridley, B., Atlas, E., Selkirk, H., Pfister, L., Montzka, D., Walega, J., Donnelly, S., Stroud, V., Richard, E., Kelly, K., Tuck, A., Thompson, T., Reeves, J., Baumgardner, D., Rawlins, W. T., Mahoney, M., Herman, R., Friedl, R., Moore, F., Ray, E., and Elkins, J.: Convective Transport of Reactive Constituents to the Tropical and Mid-Latitude Tropopause Region: I. Observations, Atmos. Environ., 38, 1259–1274, https://doi.org/10.1016/j.atmosenv.2003.11.038, 2004.

Ripoll, J.-F., Zinn, J., Jeffery, C. A., and Colestock, P. L.: On the Dynamics of Hot Air Plasmas Related to Lightning Discharges: 1. Gas Dynamics, J. Geophys. Res. Atmos., 119, 9196–9217, https://doi.org/10.1002/2013JD020067, 2014.

Rodger, C. J., Brundell, J. B., Dowden, R. L., and Thomson, N. R.: Location Accuracy of Long Distance VLF Lightning Locationnetwork, Ann. Geophys., 22, 747–758, https://doi.org/10.5194/angeo-22-747-2004, 2004.

Rodger, C. J., Werner, S., Brundell, J. B., Lay, E. H., Thomson, N. R., Holzworth, R. H., and Dowden, R. L.: Detection Efficiency of the VLF World-Wide Lightning Location Network (WWLLN): Initial Case Study, Ann. Geophys., 24, 3197–3214, https://doi.org/10.5194/angeo-24-3197-2006, 2006.

Rosenfeld, D., Lohmann, U., Raga, G. B., O'Dowd, C. D., Kulmala, M., Fuzzi, S., Reissell, A., and Andreae, M. O.: Flood or Drought: How Do Aerosols Affect Precipitation?, Science, 321, 1309–1313, https://doi.org/10.1126/science.1160606, 2008.

Rudlosky, S. D. and Shea, D. T.: Evaluating WWLLN Performance Relative to TRMM/LIS, Geophys. Res. Lett., 40, 2344–2348, https://doi.org/10.1002/grl.50428, 2013.

Rudlosky, S. D., Goodman, S. J., Virts, K. S., and Bruning, E. C.: Initial Geostationary Lightning Mapper Observations, Geophys. Res. Lett., 46, 1097–1104, https://doi.org/10.1029/2018GL081052, 2019.

Schumann, U. and Huntrieser, H.: The Global Lightning-Induced Nitrogen Oxides Source, Atmos. Chem. Phys., 7, 3823–3907, https://doi.org/10.5194/acp-7-3823-2007, 2007.

Smit, H. G. J., Straeter, W., Johnson, B. J., Oltmans, S. J., Davies, J., Tarasick, D. W., Hoegger, B., Stubi, R., Schmidlin, F. J., Northam, T., Thompson, A. M., Witte, J. C., Boyd, I., and Posny, F.: Assessment of the Performance of ECC-ozonesondes under Quasi-Flight Conditions in the Environmental Simulation Chamber: Insights from the Juelich Ozone Sonde Intercomparison Experiment (JOSIE), J. Geophys. Res. Atmos., 112, https://doi.org/10.1029/2006JD007308, 2007.

Srivastava, A., Tian, Y., Qie, X., Wang, D., Sun, Z., Yuan, S., Wang, Y., Chen, Z., Xu, W., Zhang, H., Jiang, R., and Su, D.: Performance Assessment of Beijing Lightning Network (BLNET) and Comparison with Other Lightning Location Networks across Beijing, Atmos. Res., 197, 76–83, https://doi.org/10.1016/j.atmosres.2017.06.026, 2017.

Stohl, A.: Stratosphere-Troposphere Exchange: A Review, and What We Have Learned from STACCATO, J. Geophys. Res. Atmos., 108, https://doi.org/10.1029/2002JD002490, 2003.

Sukoriansky, S., Galperin, B., and Perov, V.: Application of a New Spectral Theory of Stably Stratified Turbulence to the Atmospheric Boundary Layer over Sea Ice, Boundary Layer Meteorol., 117, 231–257, https://doi.org/10.1007/s10546-004-6848-4, 2005.

Tao, W.-K., Chen, J.-P., Li, Z., Wang, C., and Zhang, C.: Impact of Aerosols on Convective Clouds and Precipitation, Rev. Geophys., 50, https://doi.org/10.1029/2011RG000369, 2012.

van Geffen, J., Eskes, H., Compernolle, S., Pinardi, G., Verhoelst, T., Lambert, J.-C., Sneep, M., ter Linden, M., Ludewig, A., Boersma, K. F., and Veefkind, J. P.: Sentinel-5P TROPOMI NO_2 Retrieval: Impact of Version v2.2 Improvements and Comparisons with OMI and Ground-Based Data, Atmospheric Measurement Techniques, 15, 2037–2060, https://doi.org/10.5194/amt-15-2037-2022, 2022.

van Geffen, J. H. G. M., Boersma, K. F., van Roozendael, M., Hendrick, F., Mahieu, E., Smedt, I., Sneep, M., and Veefkind, J. P.: Improved Spectral Fitting of Nitrogen Dioxide from OMI in the 405–465 Nm Window, Atmos. Meas. Tech., 8, 1685–1699, https://doi.org/10.5194/amt-8-1685-2015, 2015.

Vaughan, G., Schiller, C., MacKenzie, A. R., Bower, K., Peter, T., Schlager, H., Harris, N. R. P., and May, P. T.: SCOUT-O3/ACTIVE: High-altitude Aircraft Measurements around Deep Tropical Convection, Bull. Amer. Meteor. Soc., 89, 647–662, https://doi.org/10.1175/BAMS-89-5-647, 2008.

Veefkind, J. P., Aben, I., McMullan, K., Förster, H., Vries, J., Otter, G., Claas, J., Eskes, H. J., Haan, J. F., Kleipool, Q., van Weele, M., Hasekamp, O., Hoogeveen, R., Landgraf, J., Snel, R., Tol, P., Ingmann, P., Voors, R., Kruizinga, B., Vink, R., Visser, H., and Levelt, P. F.: TROPOMI on the ESA Sentinel-5 Precursor: A GMES Mission for Global Observations of the Atmospheric Composition for Climate, Air Quality and Ozone Layer Applications, Remote Sens. Environ., 120, 70–83, https://doi.org/10.1016/j.rse.2011.09.027, 2012.

Virts, K. S. and Goodman, S. J.: Prolific Lightning and Thunderstorm Initiation over the Lake Victoria Basin in East Africa, Mon. Wea. Rev., 148, 1971–1985, https://doi.org/10.1175/MWR-D-19-0260.1, 2020.

Williams, J. E., Boersma, K. F., Le Sager, P., and Verstraeten, W. W.: The High-Resolution Version of TM5-MP for Optimized Satellite Retrievals: Description and Validation, Geosci. Model Dev., 10, 721–750, https://doi.org/10.5194/gmd-10-721-2017, 2017.

Wu, F., Cui, X., Zhang, D.-L., Liu, D., and Zheng, D.: SAFIR-3000 Lightning Statistics over the Beijing Metropolitan Region during 2005–07, J. Appl. Meteorol. Climatol., 55, 2613–2633, https://doi.org/10.1175/jamc-d-16-0030.1, 2016.

Yang, J., Zhang, Z., Wei, C., Lu, F., and Guo, Q.: Introducing the New Generation of Chinese Geostationary Weather Satellites, Fengyun-4, Bull. Amer. Meteor. Soc., 98, 1637–1658, https://doi.org/10.1175/BAMS-D-16-0065.1, 2017.

Yang, X. and Li, Z.: Increases in Thunderstorm Activity and Relationships with Air Pollution in Southeast China, J. Geophys. Res. Atmos., 119, 1835–1844, https://doi.org/10.1002/2013JD021224, 2014.

Yang, X., Sun, J., and Li, W.: An Analysis of Cloud-to-Ground Lightning in China during 2010–13, Weather Forecast., 30, 1537–1550, https://doi.org/10.1175/WAF-D-14-00132.1, 2015.

Zhang, J., Xuan, Y., Yan, X., Liu, M., Tian, H., Xia, X., Pang, L., and Zheng, X.: Development and Preliminary Evaluation of a Double-Cell Ozonesonde, Adv. Atmos. Sci., 31, 938–947, https://doi.org/10.1007/s00376-013-3104-1, 2014.

Zhang, X.: Zxdawn/Xin_ACP_2021_Convection_Effect: Version 1.1, Zenodo, https://doi.org/10.5281/ZENODO.4945560, 2021a.

Zhang, X.: Xin_ACP_2021_Convection_Effect_data, https://doi.org/10.5281/ZENODO.5154798, 2021b.

Zhang, X.: WRF-Chem-LDA-LFR, Zenodo, https://doi.org/10.5281/ZENODO.4682331, 2021c.

Zhang, X.: S5P-WRFChem, Zenodo, https://doi.org/10.5281/ZENODO.4682636, 2021d.

Zhang, X., Yin, Y., van der A, R., Lapierre, J. L., Chen, Q., Kuang, X., Yan, S., Chen, J., He, C., and Shi, R.: Estimates of Lightning NO_x Production Based on High-Resolution OMI NO_2 Retrievals over the Continental US, Atmos. Meas. Tech., 13, 1709–1734, https://doi.org/10.5194/amt-13-1709-2020, 2020.

Zhao, P., Li, Z., Xiao, H., Wu, F., Zheng, Y., Cribb, M. C., Jin, X., and Zhou, Y.: Distinct Aerosol Effects on Cloud-to-Ground Lightning in the Plateau and Basin Regions of Sichuan, Southwest China, Atmos. Chem. Phys., 20, 13 379–13 397, https://doi.org/10.5194/acp-20-13379-2020, 2020.

Zhu, Q., Laughner, J. L., and Cohen, R. C.: Lightning NO_2 Simulation over the Contiguous US and Its Effects on Satellite NO_2 Retrievals, Atmos. Chem. Phys., 19, 13 067–13 078, https://doi.org/10.5194/acp-19-13067-2019, 2019.